

N72-13678



PSU AERSP 71-4

# CASE FILE COPY

## AN INVESTIGATION OF TRANSIENT PRESSURES AND PLASMA PROPERTIES IN A PINCHED PLASMA COLUMN

By

E.K. Stover and T.M. York

Performed Under NASA Contract

NASA-SSEL 432-66(36)

Department of Aerospace Engineering  
The Pennsylvania State University  
University Park, Pa.

August, 1971

AN INVESTIGATION OF TRANSIENT PRESSURES  
AND PLASMA PROPERTIES IN A PINCHED PLASMA COLUMN

by

E. K. Stover and T. M. York

Performed under NASA Grant  
NASA-SSEL 432-66 (36)

This report is a reproduction in its entirety of the M.S. dissertation of Mr. Elmer K. Stover. It is intended as a presentation of the technical material itself and as an indication of the academic program supported by this Grant.

Department of Aerospace Engineering  
The Pennsylvania State University  
University Park, Pa.

August, 1971

## ACKNOWLEDGMENTS

The author wishes to express his gratitude to Dr. Thomas M. York for his patience in providing advice and guidance during the course of this work. The author is also grateful for having been the recipient of an NDEA Title IV Fellowship during the period September 1970 to September 1971. Financial support for this work was provided by the National Aeronautics and Space Administration under Grant NASA-SSEL 432-66(36).

## TABLE OF CONTENTS

	<u>Page</u>
Acknowledgements . . . . .	ii
List of Figures . . . . .	iv
Nomenclature . . . . .	v
Abstract . . . . .	viii
I. INTRODUCTION . . . . .	1
1.1 Statement and Discussion of Problem . . . . .	1
1.2 Previous Investigations . . . . .	2
1.3 Scope and Method of Approach . . . . .	6
II. APPARATUS AND TESTING CONDITIONS . . . . .	8
2.1 Introduction . . . . .	8
2.2 Discharge Apparatus and Auxiliary Equipment . . . . .	8
2.3 Discharge Conditions . . . . .	11
2.4 Electrical Circuit Characteristics . . . . .	12
III. DIAGNOSTIC DEVICES . . . . .	16
3.1 Introduction . . . . .	16
3.2 Rogowski Coil . . . . .	16
3.3 Voltage Probe . . . . .	18
3.4 Magnetic Field Probe . . . . .	20
3.5 Pressure Probe . . . . .	25
3.6 Luminosity . . . . .	30
IV. ANALYSIS AND DISCUSSION OF RESULTS . . . . .	34
4.1 Introduction . . . . .	34
4.2 Dynamic Current Sheet Collapse Phase . . . . .	34
4.3 Plasma Column Formation and Development . . . . .	42
V. SUMMARY AND CONCLUSIONS . . . . .	79
REFERENCES . . . . .	81
APPENDIX A . . . . .	84

## LIST OF FIGURES

<u>Figure</u>	<u>Title</u>	<u>Page</u>
1.	Discharge Apparatus Schematic	10
2.	Integrated Rogowski Coil Output	14
3.	Discharge Voltage Measurement Configurations	19
4.	Inner Divider and Total Chamber Voltage	21
5.	Typical Magnetic Field and Pressure Probe Responses on Discharge Chamber Midplane	23
6.	Discharge Chamber Current Density Profile at $t = 3.0\mu\text{sec}$	26
7.	Piezoelectric Pressure Probe Schematic	28
8.	Kerr Cell Photographic System Schematic	32
9.	Current Sheet and Plasma Column Luminosity	33
10.	Imploding Current Sheet Trajectory	35
11.	$J_z B_\theta$ , Magnetic Induction, and Current Density Profiles at $t = 3.0\mu\text{sec}$	41
12.	Plasma Column Axial Pressure Probe Records (Negative Ground)	43
13.	Plasma Column Axial Pressure Probe Records (Positive Ground)	44
14.	Reduced Plasma Column Axial Pressure	47
15.	Discharge Chamber Total Energy	56

## NOMENCLATURE

A	Cross-sectional area of one loop of Rogowski coil or magnetic field probe
B	Magnetic induction
$\dot{B}$	$\partial B / \partial t$
C	Capacitance
e	Electronic charge
E	Energy
$E_z$	Axial Electric Field Strength
f	Attenuation factor of Tektronix x 10 attenuator
I	Total circuit current
j	Current density
k	Boltzmann constant
L	Inductance
m	Mass
$m'$	MHD instability azimuthal mode number
N	Total number of particles of a given plasma species
n	Number density (Number of particles of one plasma species per unit volume)
$n'$	Number of turns or loops of Rogowski coil or magnetic field probe
P	Pressure
Q	Power
q	Total charge
R	Resistance

## NOMENCLATURE (Cont.)

$r$	Radial position coordinate referenced from the discharge chamber centerline. Positive directed outwards from axis
$\dot{r}$	$dr/dt$
$S$	Mean circumference of Rogowski coil
$T$	Temperature
$t$	Time
$V$	Voltage
$v$	Velocity
$X$	Excitation energy
$z$	Axial position in the discharge chamber
$\dot{z}$	$dz/dt$
$\gamma$	Ratio of specific heats
$\delta$	Skin thickness
$\epsilon_0$	Free space permittivity constant
$\eta$	Resistivity
$\theta$	Azimuthal position in discharge chamber
$\mu_0$	Free space permeability constant
$\nu$	Collision frequency
$\sigma$	Conductivity
$\omega_c = qB/m$	Cyclotron frequency
$\Lambda$	Ratio of impact parameter to debeye shielding distance
Subscript	
$i$	Ion
$e$	Electron

## NOMENCLATURE (Cont.)

Z	Axial
r	Radial
$\theta$	Aximuthal
+	Anode
-	Cathode
I	Inner divider
c	Chamber
o	Initial



## ABSTRACT

In this thesis the transient pinched plasma column generated in a linear Z-pinch was studied experimentally and analytically. The plasma column was investigated experimentally with several plasma diagnostics, they were; a special rapid response pressure transducer, a magnetic field probe, a voltage probe and discharge luminosity. Axial pressure profiles on the discharge chamber axis were used to identify three characteristic regions of plasma column behavior; they were in temporal sequence: strong axial pressure asymmetry noted early in plasma column lifetime (I), followed by plasma heating in which there is a rapid rise in static pressure (II) and a slight decrease static pressure before plasma column breakup (III). Plasma column lifetime was approximately 5 microseconds. The axial pressure asymmetry observed in region I was attributed to nonsimultaneous pinching of the imploding current sheet along the discharge chamber axis. The rapid heating in region II could be attributed in part to viscous effects introduced by radial gradients in the axial streaming velocity. Turbulent heating arising from discharge current excitation of the ion acoustic wave instability is also considered a possible heating mechanism.

Additional heating was observed in region III but was of a lesser order than the heating observed in region II. An energy balance conducted for the discharge chamber indicated that at least 50 percent

of the energy deposited within the discharge chamber can be attributed to radiation losses. The energy deposited in the plasma, greatest in region I, was approximately 25 percent of the discharge chamber energy but was only 2 percent of the total initial capacitor bank energy.

## CHAPTER I

### INTRODUCTION

#### 1.1 Statement and Discussion of the Problem

The pulsed plasma accelerator has been recognized as a possible propulsion system for deep space missions due to its ability to accelerate propellant to velocities on the order of  $10^5$  meters per second (1). The more conventional chemical rocket typically achieves exhaust velocities from  $3 \times 10^3$  to  $5 \times 10^3$  meters per second, too low for realistic interplanetary travel where velocity increments of  $10^4 - 10^5$  meters/second are required (1). Mission velocity increment and exhaust velocity must be of the same magnitude in order that payload mass may be realistic for a given initial system mass.

Numerous plasma accelerator geometries have been examined in an effort to understand the acceleration mechanisms active in such devices; the transfer of stored electrical energy to the gas is accomplished by the passage of extremely high electrical currents through the propellant (1). The high currents passing through the gas induce a magnetic field which interacts with the current through the  $\vec{J} \times \vec{B}$  body force resulting in gas entrainment and acceleration. A recent detailed study of the current-mass entrainment region in a linear Z-pinch device was conducted by York (2). In this particular geometry with a gas filled cylindrical chamber, the axial current flowing as a

distributed sheet between two end-wall electrodes interacts with the induced azimuthal magnetic field resulting in a radial collapse of the current sheet into a hot, dense column of plasma on the chamber centerline. The purpose of the present work is to investigate the plasma column in such a device and develop an understanding of its properties. Such an understanding of these properties is fundamental to an evaluation of the energy transfer mechanism in gas acceleration devices that utilize electrothermal, electrostatic and electromagnetic mechanisms.

## 1.2 Previous Investigations

The earliest investigations of the pinched plasma column were performed in the 1950's and early 1960's when the linear Z-pinch device was considered a potential source of fusion power. However, a low plasma column lifetime resulting from catastrophic MHD instabilities and temperature limitations imposed by column contamination from chamber walls and electrodes, precluded the possibility of a feasible Z-pinch reactor (3, 4). Experimental controlled fusion programs were then oriented toward more promising devices. Plasma gun or plasma injector research, however, was also initiated at this time for the controlled fusion effort (5). Plasma acceleration was derived in these devices from the basic  $\vec{J} \times \vec{B}$  body force, also the mechanism for linear Z-pinch acceleration. Various device geometries were considered (1) with the earliest being the coaxial accelerator in which several liters of hydrogen was accelerated to a velocity of  $1.5 \times 10^{-4}$

meters/second (5). Investigation of the pinched plasma ejected from axial orifices of various diameters was conducted with an 8-inch diameter linear Z-pinch device (6). Kerr cell photographs and magnetic search coil data were the principle diagnostics used in investigating the plasma. The velocity of the axially ejected plasma was found from these data to exceed the radial velocity inside the chamber which was approximately  $10^4$  meters/second. Thus a device such as this one could be used in developing intermittent plasma accelerators. Identification of the flow of mass within the discharge chamber and in the exhaust could not be ascertained however for a suitable diagnostic had not been developed at that time (1964). It will be noted that in addition to enabling evaluation of the flow of plasma, a pressure-sensing instrument would also enable an estimation of plasma temperature from which the thermal energy of the plasma may be deduced. This would be useful in a detailed study of plasma properties. In the present study, probing the plasma column with a suitable pressure transducer was thus paramount.

First attempts at measuring pressure in the plasma column were reported in 1956 where a piezoelectric measuring device was used (7). The discharge current was varied between 300 kiloamps and 500 kiloamps in a Z-pinch configuration with deuterium initial fill pressures ranging from 20 millitorr to 100 millitorr. The capacitor bank used for energy storage (62 $\mu$ f), was charged to either 20 kilovolts or 30 kilovolts. Thus, bank storage energy was roughly one order of

magnitude higher than the 2.5 kilojoule energy storage capacity anticipated in this study. Axial probing of the column revealed indications of pressure from 60 atmospheres to 80 atmospheres, generally increasing with initial gas fill pressure. These pressures were attributed to thermal motion. Radial pressure peaks of 120 atmospheres were measured on the chamber centerline and found to be in satisfactory agreement with the numerical results of a proposed fluid model (8). No consideration was given to variation of pressure with axial position or orientation. More recent investigations utilizing a more highly developed pressure probe (2) revealed a pronounced pressure asymmetry in the current sheet (2) and pinched column (9). Axial pressure asymmetries of several tens of atmospheres were noted in the pinched column study (9). Gas discharges were made in an 8-inch diameter device at an argon pressure of 100 millitorr, total current was approximately flat at 200 kiloamps (9).

Estimates of the energy added to the plasma were experimentally carried out in the linear Z-pinch (10, 11, 4). Andrianov (10) found that the total energy deposited in the discharge chamber at pinch, as well as the percentage of the total bank energy deposited, was a function of the initial bank energy. It was also found that the total energy deposited increases with bank voltage, whereas the percentage of energy transfer decreases. This was based upon the results of discharges varying from 40 kilovolts to 120 kilovolts using a 64 $\mu$ f capacitor bank. The percentage of energy transfer, or transfer

efficiency, was found to vary from 30 percent at 40 kilovolts to 10 percent at 120 kilovolts for 50 millitorr deuterium (10). Bodin et al. (4) found that for 350 millitorr deuterium, the transfer efficiency was roughly 25 percent at 20 kilovolts with a current rise rate identical to Andrianov's (10) at  $10^{12}$  amperes/second. Both Andrianov and Bodin found that less than 50 percent of the energy deposited in the discharge chamber was resident in the magnetic fields. Particle energies were thus calculated neglecting continuum radiation losses. Ohmic heating of the plasma was also neglected by Bodin.

A study of the energy transfer to a propagating current sheet was conducted under experimental conditions more closely approximating those of this study (11). Transmission line impedance was varied for discharges into 100 millitorr argon at 10.5 kilovolt bank voltage. Current sheet kinetic energy, gas thermal energy and magnetic field energy were evaluated at a chamber radius of 1 inch. Their sum, assuming no radiation losses and neglecting ohmic heating was found to vary between 40 percent to 60 percent of the total bank energy. The trends found in these results agree with those of Andrianov and Bodin. Plasma particle energy, kinetic energy plus thermal energy, was found to be as high as 95 percent of the discharge chamber energy for low bank energies, 1.4 kilojoules, and 60 percent at higher energies, 4.2 kilojoules. Bank energy for the present study was 2.5 kilojoules.

### 1.3 Scope and Method of Approach

The object of this investigation was to experimentally and analytically examine the pinched column, using several diagnostic techniques in an effort to identify and evaluate the following:

- (1) Partitioning of energy within the column and discharge chamber, and the resultant efficiency of energy transfer from the energy storage bank to the plasma column
- (2) Column heating, i.e. thermal energy content and heating mechanisms
- (3) Plasma and/or ion streaming in the plasma column

An outline of the logical analytical scheme is presented below. A more detailed description of the diagnostics used and their calibration will be discussed separately.

Single species plasma column number density was inferred from a one-dimensional momentum analysis in which the time rate of change of mass swept up by the current sheet is balanced by the  $\vec{J} \times \vec{B}$  body force acting on the plasma. The current sheet trajectory was found from a radial survey of the chamber using a magnetic search coil. These records indicate the regions of intense current flow ( $\dot{B}_\theta$ ). Thus, estimating the mass pickup and measuring the column radius with luminosity data, particle number density was found. Each individual plasma species, presuming full ionization, was assumed to obey the perfect gas law and be in local translational equilibrium. Plasma ion and electron temperature were then extracted from combined pressure



data and selected voltage measurements. Ion streaming was evaluated within the column, as well as at two other radial stations, from axial pressure measurements using an impact momentum transfer approximation. Total energy deposited within the discharge chamber was calculated from total voltage drop measurements across the chamber and total current, 70ka peak, inductively measured by a Rogowski coil surrounding the discharge circuit. Thus, knowing the energy in the thermalized plasma column, i.e., the random thermal kinetic energy, the axial kinetic energy and an estimation of the energy of excitation in electron energy levels, the efficiency of the device at pinch was evaluated.

Plasma heating was evaluated by estimating the change in random translational kinetic energy based on the perfect gas assumption. Viscous heating and turbulent heating mechanisms were invoked to rationalize a region of notable heating during pinched column lifetime.

Axial streaming of the plasma was evaluated from the pressure data as discussed above. Several models were evaluated in an effort to explain the observed streaming behavior which occurs early in pinched column lifetime.

## CHAPTER II

### APPARATUS AND TESTING CONDITIONS

#### 2.1 Introduction

Study of the pinched plasma column was based upon an analysis of detailed experimental measurements carried out in a linear Z-pinch device. The discharge chamber was cylindrical in shape with aluminum electrodes and pyrex side walls separating the discharge from the grounded return conductor. Application of a 10kv potential difference across the electrodes resulted in gas breakdown at the pyrex inner wall. This discharge then collapsed radially toward the chamber centerline as a result of the  $\vec{J} \times \vec{B}$  body force acting on the discharge. The Z-pinch geometry was selected for the plasma column study as it provides an intense compressive linear discharge, relative ease in analysis in comparison to more complicated configurations, i.e.,  $\theta$ -pinch, plasma focus, etcetera, in addition to relative ease in probing.

#### 2.2 Discharge apparatus and Auxiliary Equipment

The discharge apparatus consisted of three basic elements: the discharge chamber, the energy storage capacitor bank and a gas switch connecting the discharge chamber and capacitor bank. The capacitor bank was connected to the switch/discharge chamber by a transmission

line, inductance minimized and designed for constant current in an effort to maximize total chamber current flow at pinch. A sketch of the discharge apparatus is given in Figure 1.

The discharge chamber, defined by two 1/2-inch thick aluminum electrodes and a 1/2-inch thick pyrex sidewall, is 2 inches high and 5 inches in diameter. The grounded electrode, grounded sidewall and pyrex sidewall were all machined to accomodate various diagnostics for probing the plasma. The ground electrode was also machined to accept a gas plug valve which controlled the chamber discharge fill pressure. The gas switch was a discharge chamber modified by a plexiglas insert to prevent complete pinching. A number of gas ports were drilled around the periphery of the insert to allow gas from an external gas supply to diffuse between the switch plates until the critical breakdown pressure has been reached. The capacitor bank was charged with the switch at a pressure of only a few microns, low enough to hold off the 10kv maximum capacitor voltage. Injection of a slug of argon gas into the switch resulted in switch discharge and the transfer of 10 kilovolts across the discharge chamber. The discharge chamber thus electrically would break-down at the desired argon filling pressure.

The source of energy for the discharge apparatus consisted of 10 capacitor units (Aerovox Corp., Bedford, Mass.) rated at 5 microfarads and 40 nanohenries inductance per unit. The capacitors were connected in parallel by a parallel plate pulse forming network of variable

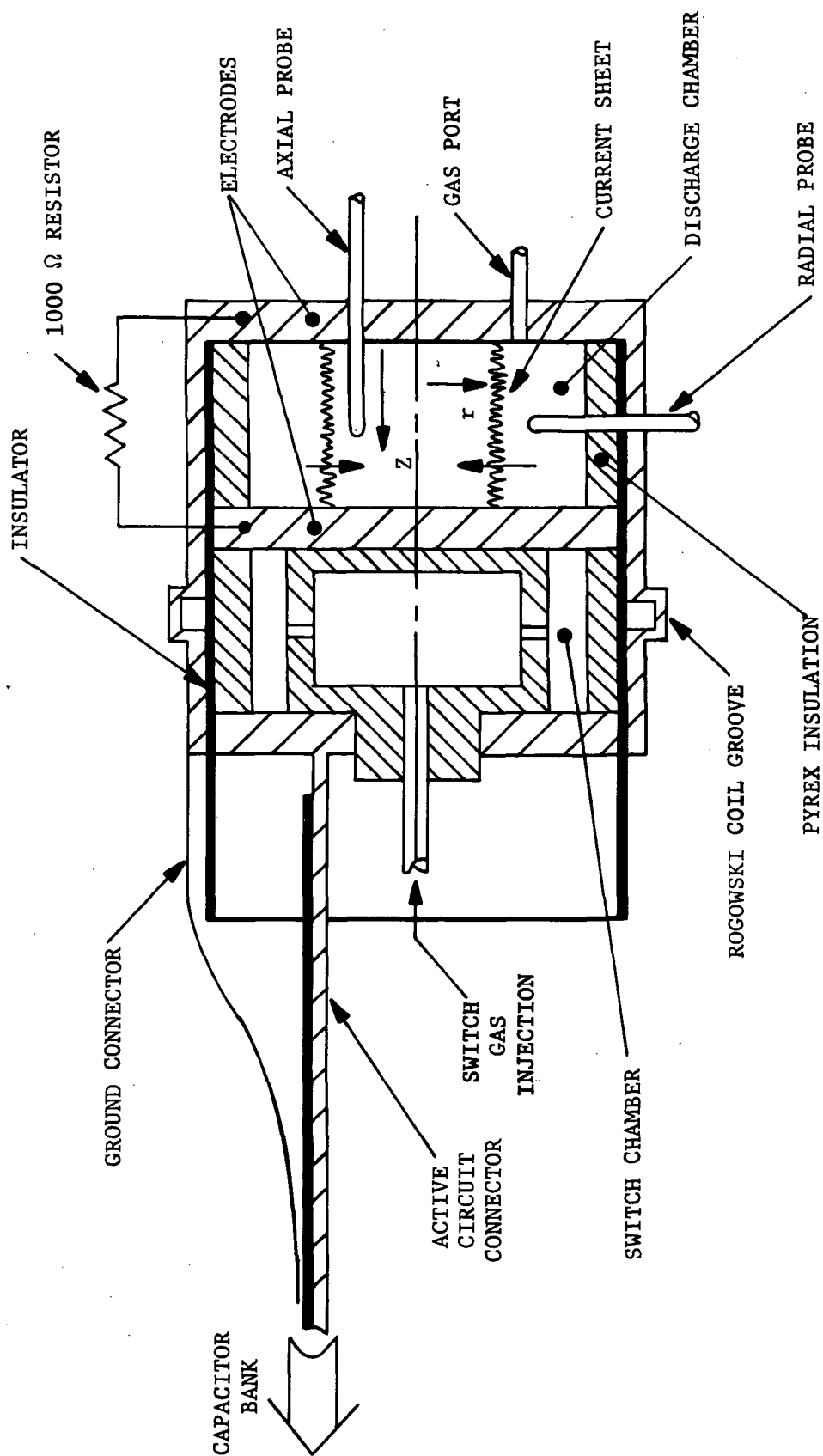


FIGURE 1: DISCHARGE APPARATUS SCHEMATIC

inductance. The inductance could be varied by raising and lowering the 1/32-inch copper ground plate. Maximum plate separation, i.e., between active and ground conductors, was approximately 3 inches. Design of the pulse forming network is discussed in Appendix A.

A Welch (1397-B) mechanical vacuum pump provided an ultimate system pressure of a few millitorr. The discharge chamber fill pressure was monitored by a Bendix Pirani gauge with a range from 1 to 2000 millitorr. The entire system was evacuated to ultimate pressure prior to each discharge.

All data with the exception of Kerr cell (light) photographs were recorded on a Tektronix Type 556 dual beam oscilloscope with Type G, H, and 1A5 preamps. The oscilloscope was shielded from undesirable discharge radiation by enclosing it within a copper screened Faraday cage. Probe connections were made with 50 ohm coaxial cable properly terminated when necessary to eliminate undesirable high frequency oscillations.

### 2.3 Discharge Conditions

The selection of discharge conditions and gas was based upon the results of previous Z-pinch experiments (2, 12, 13, 14). Argon gas was used due to its relatively low ionization potential and monatomic structure. An initial argon fill pressure of approximately 70 millitorr was used in order to obtain a thin, intense current sheet with an anticipated high gas entrainment efficiency. Current sheets a few millimeters thick with 70 percent to 80 percent

entrainment efficiency have been observed (2).

## 2.4 Electrical Circuit Characteristics

The discharge circuit parameters are summarized below:

Unit capacitance . . . . .	5 microfarads
Inductance per capacitor . . . . .	40 nanohenries
Capacitor station to station inductance . . . .	27 nanohenries
Front section inductance . . . . .	270 nanohenries
Total transmission line inductance . . . . .	510 nanohenries
Switch and network resistance . . . . .	5 milliohm (14)
Discharge chamber plus switch inductance . . .	20 nanohenries

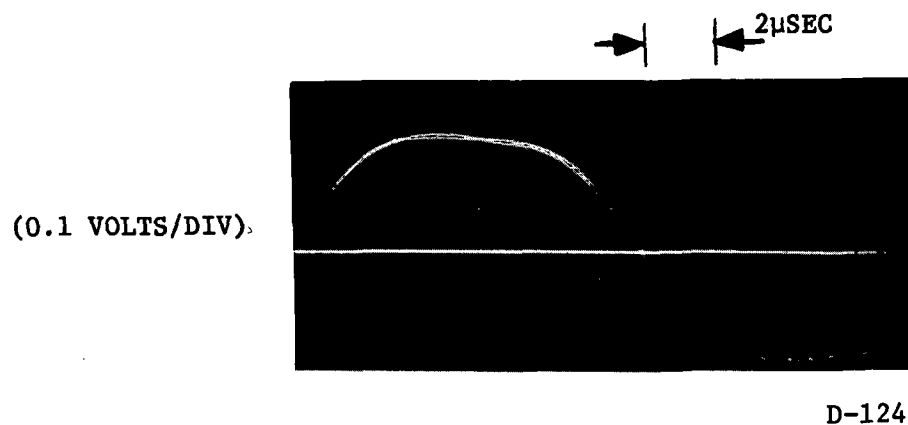
Circuit, discharge chamber and switch inductances are evaluated in Appendix A. It can be seen that the circuit impedance is reactive dominated. The transmission line inductance is more than an order of magnitude greater than the discharge chamber plus switch inductance, thus implying that the dynamics of the pinch have little effect on the total circuit current waveform.

The circuit current waveform was inductively measured by passive RC integration of the  $dI/dt$  proportional signal output from a Rogowski coil wrapped around the switch chamber. Rogowski coil calibration was accomplished by experimentally evaluating the constant of proportionality between the oscilloscope trace voltage and total circuit current. This proportionality constant is a function of integrating circuit RC, coil geometry and any voltage attenuation in the basic circuit.

The basic current waveform for plasma column study should have several distinct features in contrast to the damped sinusoidal current produced in a lumped LRC circuit. First, the current waveform should have a high initial rise rate to insure a sharp, intense discharge (14) necessary for efficient energy transfer from bank to plasma (4). The imploding current sheet should not pinch before current peak to insure peak power transfer to the discharge chamber. In addition, the current waveform should not drop off during column lifetime, approximately 5 $\mu$ sec, for the same reason. A constant current during column life would also simplify analysis of the plasma column and was a design consideration.

The current rise rate was maximized by minimizing transmission line inductance wherever possible. Initial current rise rate was estimated to be  $2 \times 10^{10}$  amps/second. The pulse waveform was kept as nearly constant as possible after initial rise by properly spacing the capacitor units with parallel plate transmission line. An 8-inch separation between capacitor active posts was found to give a repeatable, acceptably constant pulse at 70ka. A sample integrated Rogowski coil oscilloscope trace is given in Figure 2. Transmission line plate separation was kept as low as possible, approximately 1/4-inch, to minimize inductance as noted above.

Magnetic field probing of the discharge chamber and Kerr cell photographs indicated a current sheet with a slight tilt angle and a



CALIBRATION:  $4.1 \times 10^5$  AMPERES/VOLT

FIGURE 2: INTEGRATED ROGOWSKI COIL OUTPUT



noticeable diffuse current region near the discharge chamber anode.

Current sheet pinch was observed to occur at approximately  $3.7\mu\text{sec}$

## CHAPTER III

### DIAGNOSTIC DEVICES

#### 3.1 Introduction

The experimental data gathered in this study of the pinched plasma column were acquired by the application of a number of plasma diagnostic techniques (15, 16, 17). Relative to their importance, the operation and calibration of each of these diagnostics will be briefly discussed.

Basically two types of diagnostic tools were employed. Those which were inserted into the discharge chamber, i.e., magnetic field, pressure, voltage (inner divider), and those fixed external to the discharge, i.e., voltage (total discharge chamber), Rogowski coil and luminosity. Care was necessarily taken to properly protect the magnetic field and pressure probes in the severe thermal environment of the plasma column without adversely affecting probe performance. As noted above, all experimental data with the exception of luminosity pictures were photographically recorded on 3-1/4-inch by 4-1/4-inch prints taken from a polaroid camera mounted on the screen of a type 556 Tektronix dual beam oscilloscope.

#### 3.2 Rogowski Coil

Total discharge current was obtained from a Rogowski coil of standard design discussed in References 16 and 17. In order that the Rogowski coil would enclose the total discharge current, it was designed to fit into a mechanical groove machined into the grounded

shell of the discharge apparatus. Basically the Rogowski coil is a multiloop solenoid bent into the shape of a torus, see Figure 3 Reference 15 . Passage of a time varying current through the coil hoop induces an emf across the coil output leads, as per Faradays Law. When properly wound, this output is independent of the spatial distribution of the current. The emf generated across the Rogowski coil leads was rather high, approximately 70 volts, and thus required the use of heavy formvar coated copper wire for fabrication to prevent the possibility of loop to loop arcing. The coil was protected from the grounded shell by wrapping the toroidal coil in electrical insulating tape.

Integration of the Rogowski coil output signal with an appropriate RC integrator yielded the total discharge current. Integrator R and C were selected such that RC was at least a magnitude greater than the time of the event observed (17). This is necessary to reduce RC decay distortion effects on the signal. Only the first half of the current pulse was of interest,  $10\mu\text{sec}$ , thus RC was chosen to be  $110\mu\text{sec}$ . A 50 ohm terminator was connected to both the Rogowski coil outlet and the RC integrator inlet. In addition, a voltage attenuator with an attenuation factor,  $f$ , of 5.2 was included in the Rogowski coil circuit to reduce the unintegrated Rogowski coil output voltage to a more reasonable value.

Calibration of the Rogowski coil was achieved by experimentally evaluating constants in the theoretical expression for the ratio of coil

output voltage to total current (17)

$$\frac{V_{RC}}{I} = \frac{1}{f} \frac{\mu_o A n'}{SRC} = \frac{k}{fRC} \quad , \quad [3.1]$$

where  $f$ ,  $R$  and  $C$  had been carefully measured. Knowing the total charge flowing in one-half cycle from the basic definitions of capacitance and current,  $k$  may be reduced to an integral expression for the oscilloscope output. Evaluation of this integral over the first half cycle thus gives the desired calibration factor. The integrated Rogowski coil signal was found to have excellent shot to shot reproducibility.

### 3.3 Voltage Probe

Measurements were taken of the discharge chamber voltage due to their value in establishing an energy balance within the discharge chamber. Indicated in Figure 3 are the two probing configurations used in this study. Data from both configurations were taken with a high impedance Tektronix type P6013A probe rated for 12kv peak.

From the  $V_I$  configuration, hereafter referred to as the inner divider configuration, only the resistive voltage drop across the current sheet or plasma column was measured since the voltage probe current path does not enclose the discharge current magnetic flux. As a result, the  $V_I$  measurements were useful for estimating ohmic heating in the plasma. The voltage probe as noted in Figure 3 was

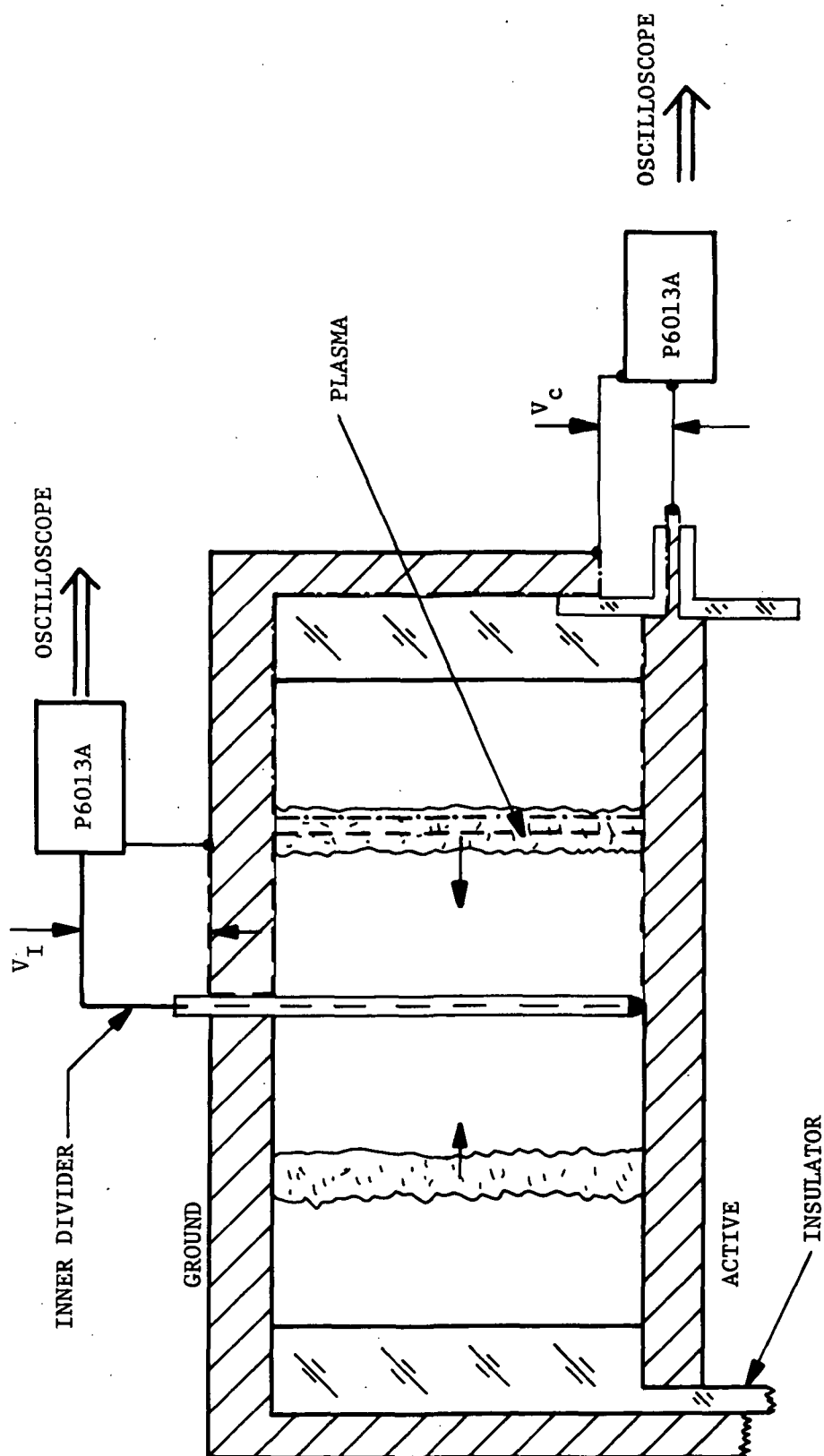


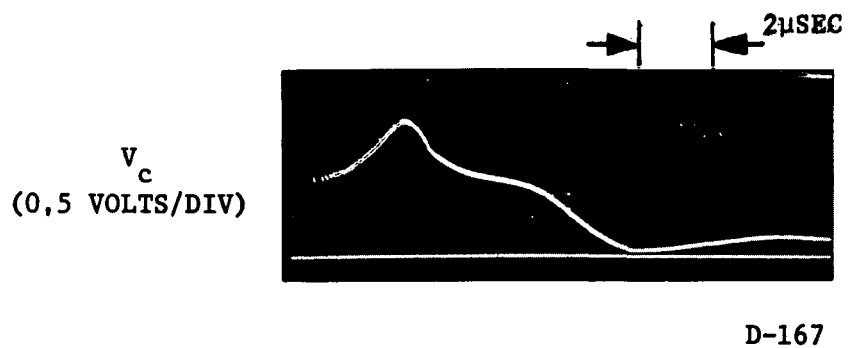
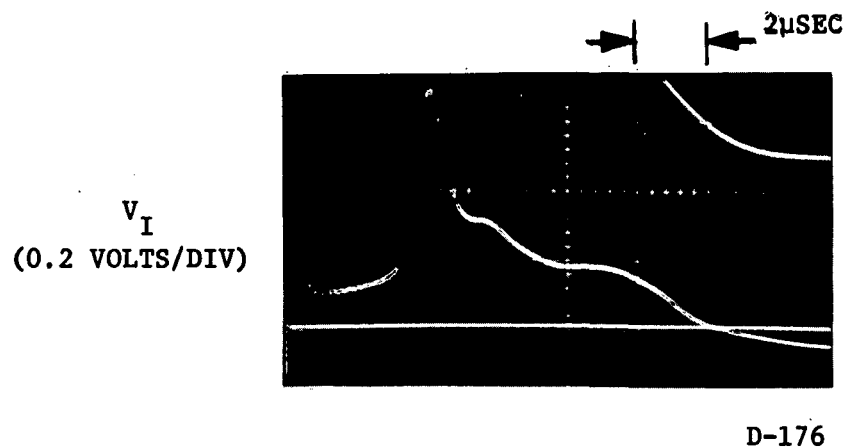
FIGURE 3: DISCHARGE VOLTAGE MEASUREMENT CONFIGURATIONS

connected to the ground electrode by a divider conductor with a nylon covering which screwed into the hot plate. Probe output was fed directly into the oscilloscope.

The  $V_c$  configuration, hereafter referred to as the total voltage configuration, can in conjunction with total current provide a measurement of the total energy deposited within the discharge chamber. It can be seen from Figure 3 that in this configuration the voltage probe circuit will include discharge chamber magnetic flux as well as the resistive drop  $V_I$  across the current sheet or plasma column. Thus knowing plasma particle energy and magnetic field energy, both of which will be discussed in the following sections, the system energy loss through radiation may be inferred. Both inner divider and total voltage records are presented in Figure 4.

### 3.4 Magnetic Field Probe

The magnetic field probe provided data that were fundamental to most analyses carried out in this study. Such data provided identification of the current sheet trajectory, basic information for calculation of the current density distribution, and accordingly provided an estimation of the plasma column number density and an estimation of magnetic field energy. The theory and operation of magnetic field probes has been reported in the literature (16). Basically, the probe is a closed multiturn electrically conducting coil which operates on the magnetic induction principle as stated by



CALIBRATION: 1000 VOLTS/VOLT OSCILLOSCOPE

FIGURE 4: INNER DIVIDER AND TOTAL CHAMBER VOLTAGE

Faradays Law. The coil emf generated by an  $n'$  loop coil of cross-sectional area  $A$  per turn is given by

$$\dot{V}_{B_{\theta}} = n'A \frac{\partial B_{\theta}}{\partial t} , \quad [3.2]$$

where  $A$ , which is normal to  $B_{\theta}$ , was selected so that  $B_{\theta}$  field gradients across  $A$  would be small enough to provide good spatial resolution. The leads from the sensing coil were tightly twisted to minimize undesirable flux threading area. The probe was wound from heavy coated formvar wire to prevent shorting. The  $B_{\theta}$  probe output voltage [3.2] identified regions of intense current flow and thus the current sheet trajectory. A typical  $\dot{B}_{\theta}$  record is presented in Figure 5 with the sensing coil positioned on the chamber midplane at radial station  $r = 1/2$  inch.

Passive RC integration of the magnetic field probe output [3.2] yields a signal voltage proportional to the magnetic induction  $B_{\theta}$  (16)

$$\begin{aligned} V_{B_{\theta}} &= \frac{1}{RC} \int \dot{V}_{B_{\theta}} dt \\ &\approx \frac{A}{RC} n' B_{\theta} . \end{aligned} \quad [3.3]$$

The magnetic field probe was fabricated by wrapping two turns of #28 heavy formvar coated copper wire about a #39 drill shank. The cross-sectional area per loop was thus  $5.08 \times 10^{-6}$  meters squared. Probe life was insured by placing the probe in a one foot length of 5 millimeter pyrex tubing fused close at one end to provide a vacuum seal. The output was terminated with a 50 ohm resistor to attenuate



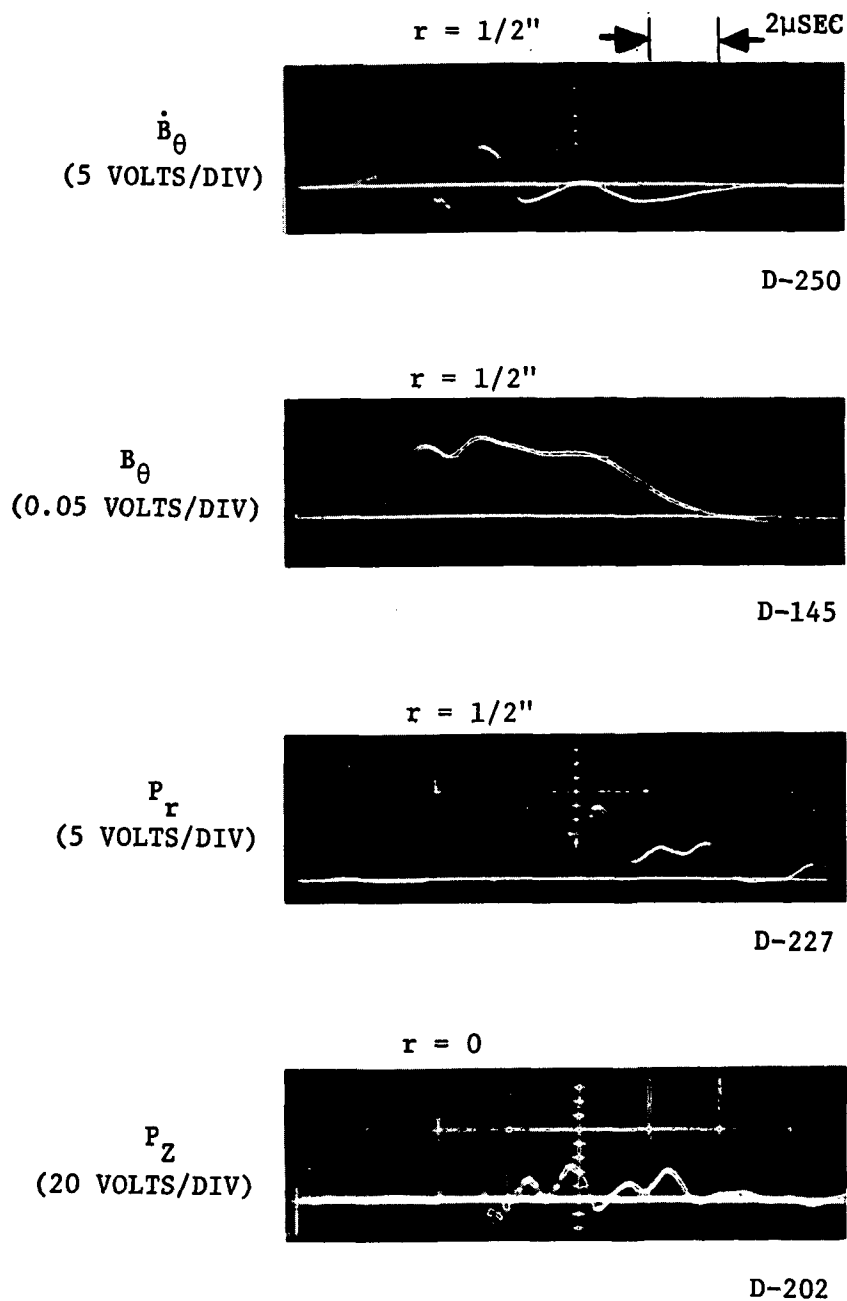


FIGURE 5: TYPICAL MAGNETIC FIELD AND PRESSURE PROBE RESPONSES  
ON DISCHARGE CHAMBER MIDPLANE

undesirable high frequency oscillation in the signal. Integrator RC, selected using the criteria discussed in section 3.2, was calibrated to be 95 $\mu$ sec. Potential sources of probe error were estimated to be small (12). A sample  $B_\theta$  oscilloscope trace is given in Figure 5 with the sensing coil positioned on the discharge chamber midplane at a radial position  $r = 1/2$  inch.

The probe was calibrated by discharging the capacitor bank, charged to 2.5 kilovolts, through an aluminum shorting post connecting the chamber electrodes. Knowing coil position and discharge current the magnetic field was inferred from Amperes law

$$B_\theta = \frac{\mu_o I}{2\pi r} \quad [3.4]$$

for a straight conductor, and then compared with oscilloscope output. The experimental calibration factor obtained from [3.4] was found to agree within 6 percent of the theoretically determined calibration factor given by [3.3].

$\dot{B}_\theta$  data were taken on the discharge chamber midplane at radial positions  $r = 0, 1/6, 1/8, 1/4, 1/2, 1, 1-1/2$  and  $1-3/4$  inches and at stations  $1/2$  inch on each side of midplane at  $r = 1/2$  inch. Axial variations in  $\dot{B}_\theta$  were taken at  $r = 1/2, 1$  inches.  $B_\theta$  data were taken only on the discharge chamber midplane at radial positions  $r = 0, 1/16, 1/8, 1/4, 1/2, 3/4, 1, 1-1/4, 1-1/2$  and  $1-3/4$  inches.

Current density profiles of the discharge chamber were generated from the  $B_\theta$  measurements using Amperes law in a one-dimensional

current flow approximation,

$$J_z \approx \frac{1}{\mu_0 r} \frac{\partial(rB_\theta)}{\partial r} \quad . \quad [3.5]$$

Magnetic field variations were assumed to be entirely radial, despite the existence of a slight current sheet tilt. A current density profile evaluated at  $t = 3.0\mu\text{sec}$  after discharge initiation is presented in Figure 6. Integration of this profile and a similar profile at  $2.5\mu\text{sec}$  yielded, as a check, total chamber current within 6 percent of the Rogowski coil calibration value. Such agreement was considered satisfactory.

### 3.5 Pressure Probe

A piezoelectric pressure sensing probe was constructed based on the design procedure developed by York (17) for making plasma pressure measurements on a submicrosecond time scale. The value of using such a diagnostic lies in its ability to identify regions of mass accumulation and mass streaming as well as enabling estimation of both total plasma temperature and the magnitude of mass streaming in the plasma column.

Briefly, the pressure probe design was based upon the piezoelectric effect in which certain materials possess the ability to generate an electrical potential when subjected to a mechanical stress. This potential, modified by the components of the probe circuit, was then recorded on an oscilloscope. With an experimentally determined calibration factor, crystal surface pressure can be inferred.

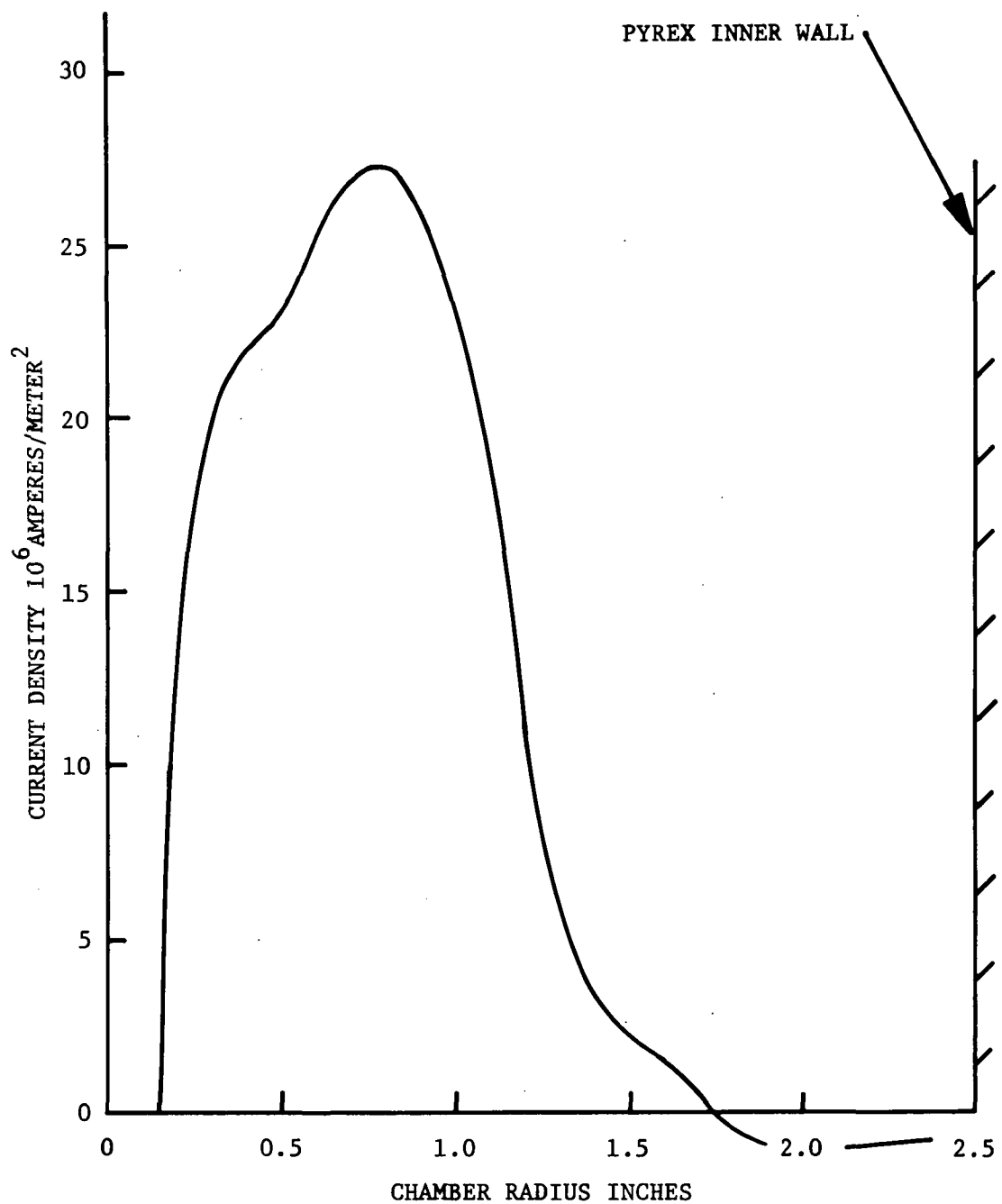


FIGURE 6: DISCHARGE CHAMBER CURRENT DENSITY PROFILE  
AT  $t = 3.0\mu\text{sec}$

Basic design criteria were focused on the construction of a probe with submicrosecond rise times and with minimal distortion of the signal by longitudinal and lateral stress waves propagating throughout the probe. Consideration was also given to protection of the probe in the discharge environment and to minimization of inductive effects on the probe signal. Acceptable rise time and oscillatory behavior were obtained with a .015 inch thick PZT-5 crystal of 5/32-inch diameter (Clevite Corporation) bonded to a 1-inch length stainless steel backing rod electrically insulated from the outer conductor, Figure 7. The probe was epoxied into an 8mm pyrex jacket and the piezoelectric crystal was coated with a layer of #74 scotch insulating tape and a thin layer of epoxy for protection against the discharge. The epoxy coating was kept thin to prevent introduction of unacceptable time delays. Induction effects were minimized by coaxial construction of the probe circuit.

The pressure probe was experimentally calibrated using the constant pressure produced by reflected shock waves generated in a simple shock tube. The probe face was mounted flush on the end plate of the ambient driven section. The driven section was separated from the driver section by an aluminum foil diaphragm which burst at an argon driver pressure of 63 psia. Driver and driven section lengths were each 3 feet in length. The shock tube diameter was 1-1/8 inches I.D. Theoretical determination of the pressure behind the reflected shock wave using simple shock tube theory (18), resulted in a calibration factor of 0.36 volts per atmosphere. This is roughly one-half the

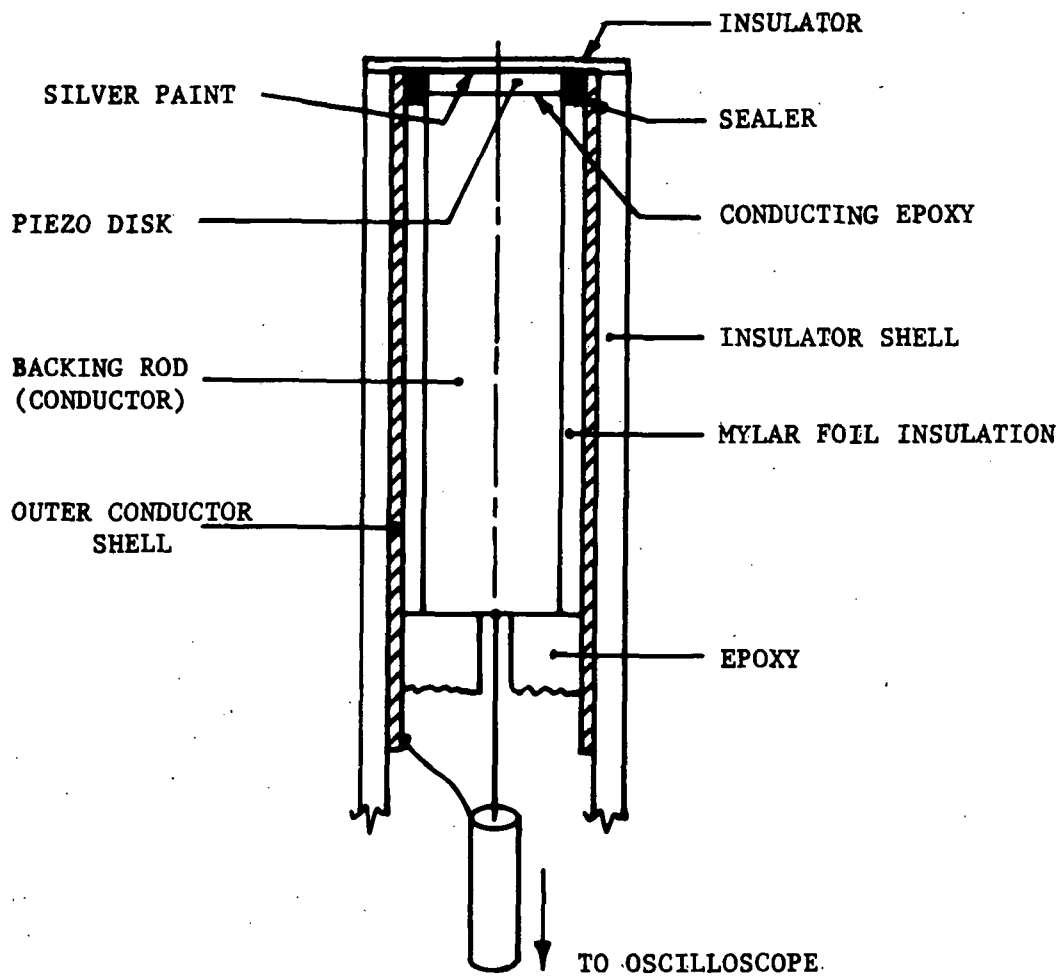


FIGURE 7: PIEZOELECTRIC PRESSURE PROBE SCHEMATIC

calibration factor determined from the theoretical probe performance. This discrepancy was attributed to losses in probe performance inherent in probe fabrication. The calibration factor 0.36 volts per atmosphere was used in reducing all pressure probe data.

The discharge chamber was probed axially and radially with the pressure probe. Radial probing was restricted to the discharge chamber midplane. Both sides of the chamber centerline were probed; with the probe crystal facing the imploding current sheet (+r) and the crystal facing leeward to the imploding current sheet (-r). Radial pressure records taken at  $r = +1/2$ -inch are presented in Figure 5. Comparison with the  $\dot{B}_0$  trace also taken at  $r = 1/2$ -inch indicates that the current conduction region precedes the region of predominant mass accumulation as noted by Fillipov (7) and York (2), although the data presented here are not simultaneous.

Axial probing of the discharge chamber was performed at radial stations  $r=0$ ,  $1/2$  and  $1$  inches. Axial stations selected were  $h = 0$ ,  $1/2$ , and  $1-1/2$  inches referenced to the cathode when the power supply was connected for negative ground, and to the anode when connected for positive ground, Figure 1. The polarity of the chamber was reversed to enable evaluation of plasma streaming.

The anode mounted pressure probe at station  $r = 0$  responds to the total static gas pressure and is assumed to be related to the kinetic temperature of the gas by the perfect gas law

$$P_{Z+} = nk(T_e + T_i) . \quad [3.6]$$

The plasma column was assumed to be 100 percent singly ionized based on a microwave study (12) and spectroscopic results (19). These results indicated that some second level ionization may exist in the column. This has not been confirmed, however, thus the simple singly ionized assumption was used.

The strong axial pressure asymmetry suggests applicability of a blunt body hypersonic analysis as used by York (2) in analyzing radial pressure data. The predicted stagnation surface pressure is

$$P = \left[ 1 - \frac{1}{2} \left( \frac{\gamma-1}{\gamma+1} \right) \right] nmv^2 ,$$

and for  $\gamma = 1.2$  which approximates the plasma (20)

$$P \approx nmv^2 . \quad [3.7]$$

Stagnation pressures were measured from the cathode mounted, axial probing positions (negative ground). Due to the large difference in mass between the ions and electrons the streaming velocity of the ions was thus determined from [3.7] to be

$$v_i \approx \left[ \frac{P}{n_i m_i} \right]^{1/2} . \quad [3.8]$$

### 3.6 Luminosity

Photographic reproductions of the discharge enabled visual verification of current sheet and plasma column behavior. Plasma current sheet pinch time in addition to plasma column life and geometry were inferred from these luminosity exposures.



Unobstructed photographs were taken of the discharge using a Kappa Scientific Kerr cell photographic system sketched in Figure 8. A discharge chamber with a cutout on one side for viewing, but similar in every respect to the configuration discussed in Chapter II, was adapted to the existing device. The Kerr cell was driven by a 32 kilovolt power supply and had an exposure time of 50 nanoseconds. Kerr cell transparency, which serves as an analog to a mechanical shutter, was controlled by a time delayed signal originating from the oscilloscope. Black and white 4 x 5 prints were taken with a Graflex 45 bellows camera and 35 mm color slides were taken with a Pentax Spotmatic. Prints taken at  $t = 2.5\mu\text{sec}$  and at pinch,  $3.75\mu\text{sec}$ , are shown in Figure 9.

Examination of the Kerr cell photographs indicates a well defined current sheet for all times up until pinch. As would be anticipated,  $\dot{B}_\theta$  peaks and Kerr cell prints were in good agreement indicating that luminosity can be associated with intense current flow. Strong radial electric fields precluded significant separation between plasma ions and electrons, thus the effective plasma column radius was based upon Kerr cell photographs. Column radial oscillatory behavior was noted prior to breakup of column toward sidewalls at  $t = 9\mu\text{sec}$ . No photographic evidence of either  $m' = 0$  or  $m' = 1$  MHD instabilities leading to plasma column breakup was observed.

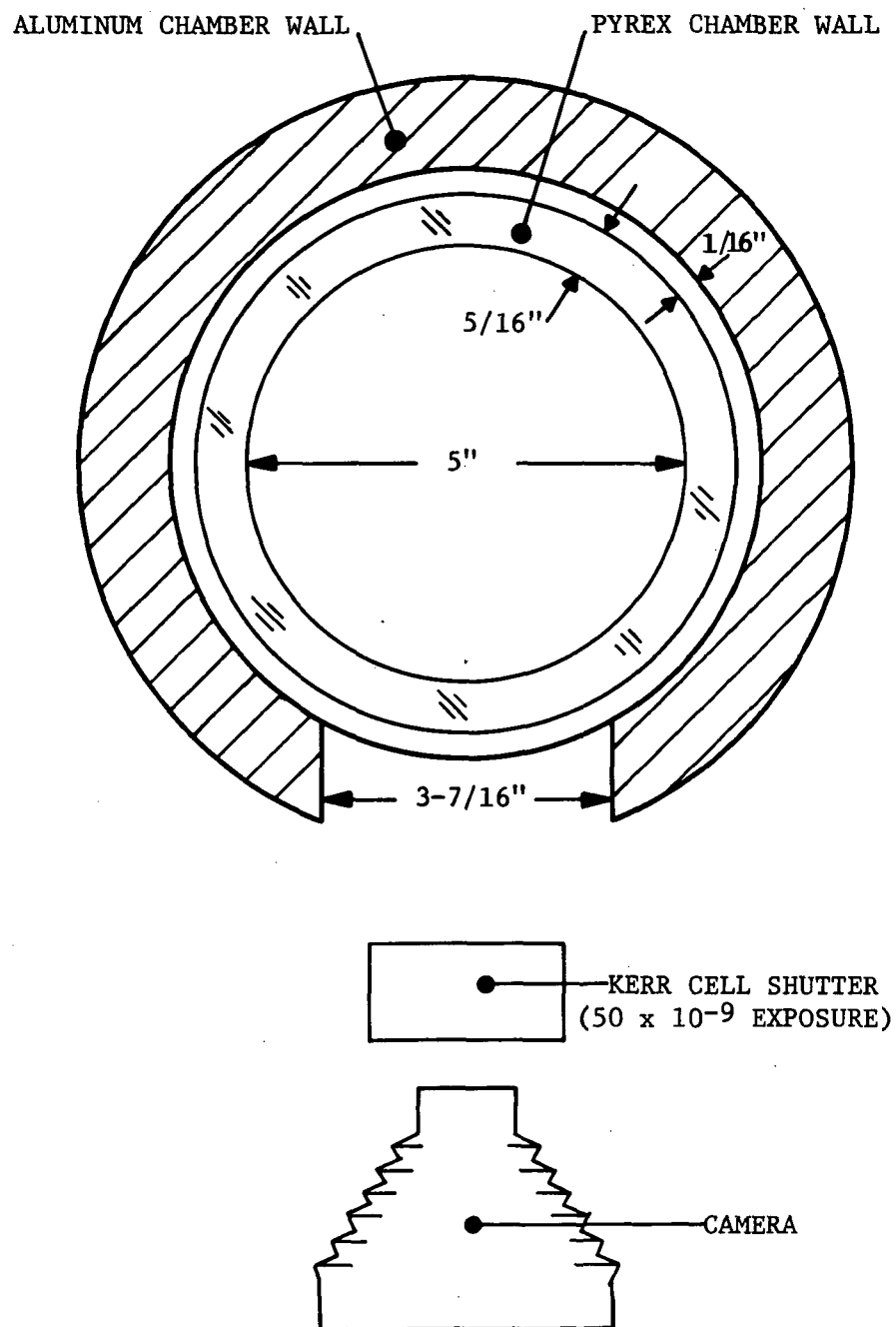
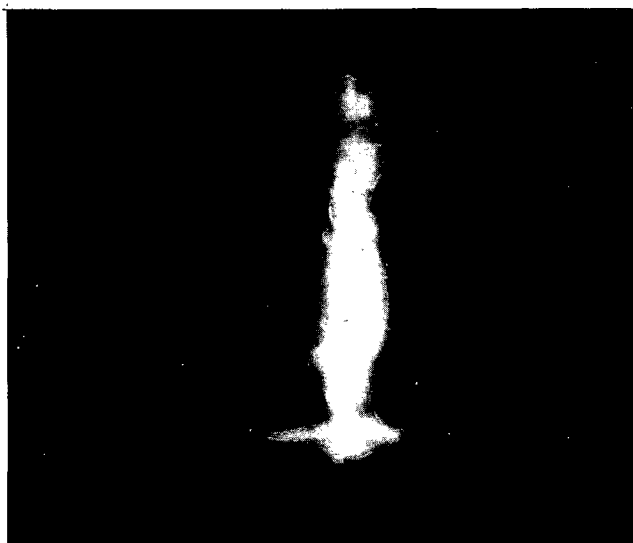


FIGURE 8: KERR CELL PHOTOGRAPHIC SYSTEM SCHEMATIC

$t = 2.5\mu\text{SEC}$ 

D-21L

 $t = 3.75\mu\text{SEC}$ 

D-28L

FIGURE 9: CURRENT SHEET AND PLASMA COLUMN LUMINOSITY

## CHAPTER IV

### ANALYSIS AND DISCUSSION OF RESULTS

#### 4.1 Introduction

Analysis of plasma column behavior was based upon experimental data obtained from the various plasma diagnostic tools discussed in the previous chapter. The dynamic implosion phase of the pinch phenomena was considered first in order that gas entrainment and energy resident in the gas immediately prior to pinch could be evaluated. Post pinch conditions were then established using pressure, magnetic field and voltage data in conjunction with the plasma column number density obtained from the mass pick-up calculations and luminosity data. Plasma streaming, associated with the axial pressure asymmetry, will be discussed with consideration given to possible acceleration mechanisms. Pronounced heating noted to follow termination of column pressure asymmetry will also be discussed. An overall system detailed energy balance will be performed and extrapolated as an indicator of propulsion system performance.

#### 4.2 Dynamic Current Sheet Collapse Phase

The current sheet radial trajectory presented in Figure 10 was evaluated from midplane  $\dot{B}_0$  peak arrival times, and mass arrival times defined from the radial pressure records by the time of pressure discontinuity arrival. It can be seen that for chamber radii greater

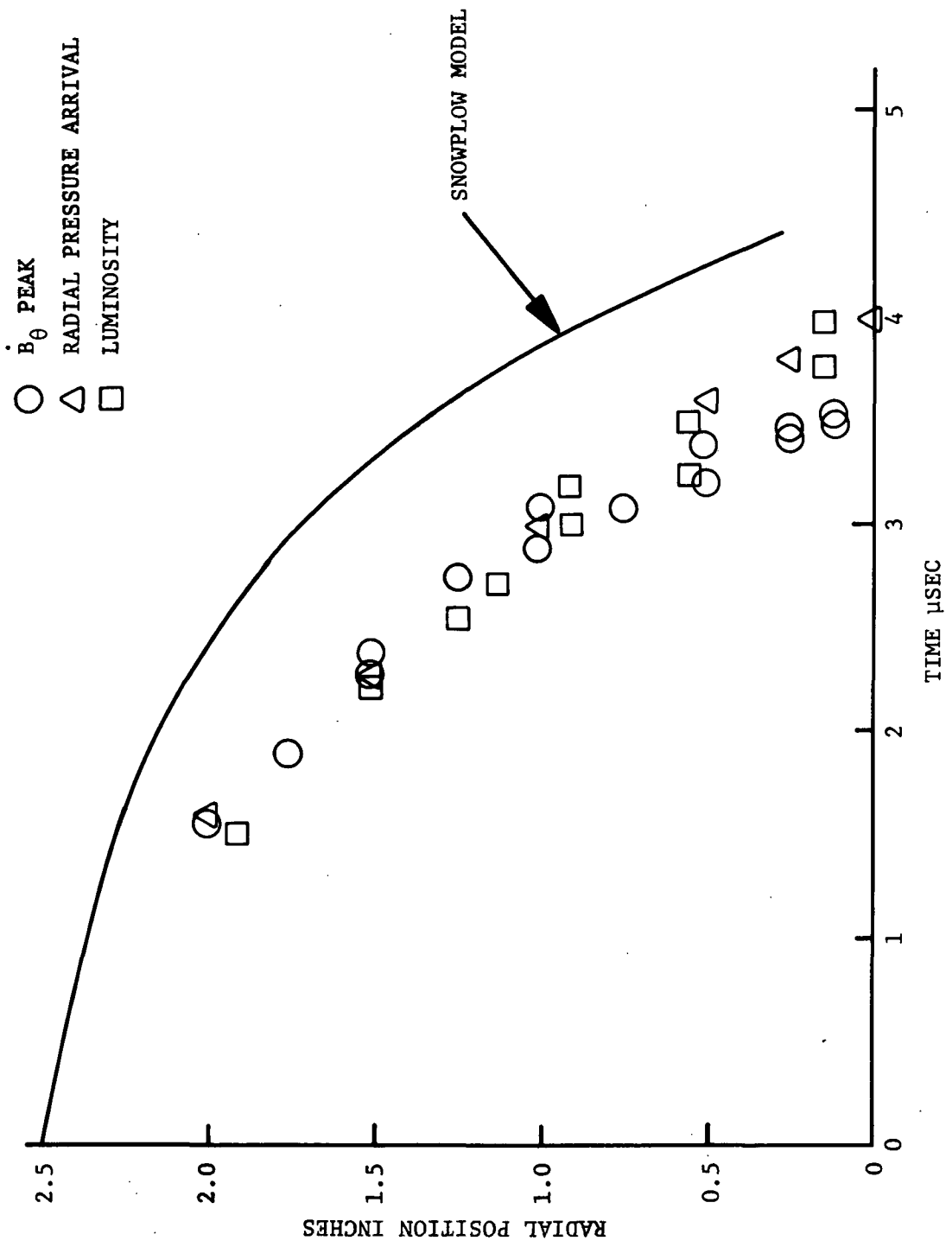


FIGURE 10: IMPLoding CURRENT SHEET TRAJECTORY

than 1 inch, the regions of current flow ( $\dot{B}_\theta$  peak) and mass entrainment are in reasonable proximity, indicating a merging of these regions. However, the pressure records indicate that the mass entrainment region lies to the rear of the current sheet  $\dot{B}_\theta$  peak. Such current sheet behavior has been noted by York (2) and Fillipov (7). For chamber radii less than 1 inch a divergence in the trajectories of  $\dot{B}_\theta$  peak and radial pressure was noted, with the  $\dot{B}_\theta$  peak pinch time ( $3.5\mu\text{sec}$ ) preceding the radial pressure pinch time ( $4\mu\text{sec}$ ) by  $0.5\mu\text{sec}$ . Luminosity data also included in Figure 10 confirmed the sheet dynamics noted above for chamber radii greater than 1 inch. For radii less than 1 inch the position of the luminosity front was found to fall between peak  $\dot{B}_\theta$  and radial pressure rise.

A simplified model for the dynamics of the current sheet in a one-dimensional Z-pinch was proposed by Rosenbluth (21) in 1954. In this particular scheme, called the snowplow model, the rate of change momentum of the entrained mass is balanced by the  $\vec{J} \times \vec{B}$  body force acting on the current sheet particles. The plasma is assumed to be incompressible and have an infinite conductivity, thus the current sheet consisting of entrained mass and current carriers must be infinitesimally thin. Equally important is the assumed impermeability property of the current sheet in which all of the gas overrun by the current sheet is entrained. The resultant differential equation for sheet

position,  $r$ , in mks units is

$$\frac{d}{dt} \left[ (r_o^2 - r^2) \frac{dr}{dt} \right] = - \frac{\mu_o I^2}{4\pi^2 \rho_o r} \quad . \quad [4.1]$$

From Figure 2 it can be seen that for times prior to pinch, i.e., 3.5 $\mu$ sec to 4.0 $\mu$ sec, the current waveform can be approximated by a linear relation

$$I = \dot{I} t \quad ,$$

where the average  $\dot{I}$  was estimated to be  $3 \times 10^{10}$  amperes/second. Due to the nonlinear nature of the above momentum equation, the solution was obtained numerically. The linear current rise case was considered by Black, (14), who performed the numerical integration. Nondimensionalized trajectories were obtained. Using the above stated  $\dot{I}$ , the discharge chamber radius,  $r_o = 6.35 \times 10^{-2}$  meters and the initial fill mass density for 70 millitorr argon pressure,  $\rho_o = 1.58 \times 10^{-4}$  kg/m<sup>3</sup>, the snowplow trajectory was computed and is presented in Figure 10. Pinch time predicted by snowplow theory occurs at approximately 4.5 $\mu$ sec, 1 $\mu$ sec later than  $\dot{B}_o$  and 0.5 $\mu$ sec later than mass. It should be noted that the snowplow model assumes 100 percent mass pickup by the current sheet. Previous studies have shown that the current sheet is not a perfect snowplow but rather permeable (1). Thus if a permeability factor is assumed for the snowplow better agreement should be obtained with the experimental data, in particular the pressure data. The leaky snowplow will pinch faster for the

accelerated mass will be smaller. Identifying an average acceleration for both the leaky model and the ideal model based on percentage of entrainment it was estimated that the percentage entrainment required to match mass pinch would be approximately 79 percent. Based on more precise calculations of mass entrainment to be discussed in ensuing paragraphs, it will be shown that the percentage entrainment of gas was in fact 80 percent. Thus the time-to-pinch of entrained mass should be closely approximated by a leaky snowplow model. Detailed sheet structure cannot be predicted by the snowplow model, however, due to the finite conductivity of the plasma, and the basic discrepancy in the relative position of current and mass within the sheet.

Before attempting to analyze plasma column data the mass entrained by the imploding current sheet must be evaluated as well as the energy resident in the imploding gas immediately prior to pinch. Mass entrainment was estimated from Newton's second law where the time rate of change of momentum of gas entrained by the current sheet is equal to the  $\vec{J} \times \vec{B}$  body force per unit volume integrated over an appropriate volume,  $V$ , as

$$\frac{d}{dt} (m_i v_{ri}) = \int_V J_z B_\theta dV \quad . \quad [4.2]$$

Azimuthal symmetry is assumed for the system and for this particular case  $v_{ri}$ , the ion radial velocity, is positive when directed toward the discharge chamber centerline. Letting  $h$  be the height of the



chamber and  $dA$  an incremental element of surface area normal to  $h$ , multiplying both sides by  $dt$  yields

$$d(m_i v_{ri}) = h \left[ \int_A J_Z B_\theta dA \right] dt .$$

For the purpose of step calculation, this equation can be expressed in incremental form as

$$m_i \Delta v_{ri} + v_{ri} \Delta m_i = h \left[ \int_A J_Z B_\theta dA \right] dt , \quad [4.3]$$

thus the mass pick-up over time interval  $\Delta t$  is

$$\Delta m = \frac{h \left[ \int_A J_Z B_\theta dA \right] \Delta t - m_i \Delta v_{ri}}{v_{ri}} , \quad [4.4]$$

where  $m_i$ ,  $v_{ri}$  and  $\int_A J_Z B_\theta dA$  become averaged quantities over the time interval  $\Delta t$ . The body force area integral was evaluated from the discharge chamber centerline to the rear of the mass entrainment region estimated from the radial pressure records. The  $J_Z B_\theta$  profiles generally had non-zero values at stations forward of the leading edge of the mass accumulation region. This region was included in the momentum balance, however, due to the accepted existence of a radial electric field (2) which can transmit the  $\vec{J} \times \vec{B}$  force from the current

carrying electrons of negligible mass to the ions. These fields, experimentally observed in (2, 12) were found to be sufficient in magnitude to accelerate overrun rest ions to sheet velocity.

Current density,  $J_z$  and magnetic field,  $B_\theta$  were obtained as outlined in Chapter III. A typical  $J_z B_\theta$  profile is presented in Figure 11 as well as the  $J_z$  and  $B_\theta$  profiles. Velocities  $v_{ri}$  and  $\Delta v_{ri}$  were obtained from radial pressure front trajectories from Figure 10. Due to difficulty encountered in extracting magnetic field data at times less than  $t = 1.5\mu\text{sec}$ , the starting calculation was performed over the first  $1.5\mu\text{sec}$  using the  $\vec{J} \times \vec{B}$  integral at  $t = 1.5\mu\text{sec}$ . Subsequent time intervals chosen were  $0.5\mu\text{sec}$  up to  $t = 3.0\mu\text{sec}$ , and  $0.25\mu\text{sec}$  intervals for  $t > 3.0\mu\text{sec}$  until pinch. Total mass pick-up was found to be  $8 \times 10^{-8}$  kg, 80 percent of the initial total mass of the system. This corresponds to  $1.2 \times 10^{18}$  argon particles. From luminosity results the column radius at  $t = 4.0\mu\text{sec}$  which corresponds to mass pinch was estimated to be 0.2 inches. This corresponds to a plasma column number density of  $2.94 \times 10^{23}$  particles/ $\text{m}^3$ . These results are in agreement with plasma column radius and electron number density inferred spectroscopically from a linear Z-pinch study with argon at a higher fill pressure (22). Capacitor bank energies were identical at 2.5 kilojoules.

The radial kinetic energy per particle was estimated just prior to pinch, from:

$$W_i = 1/2 m_i v_{ri}^2$$

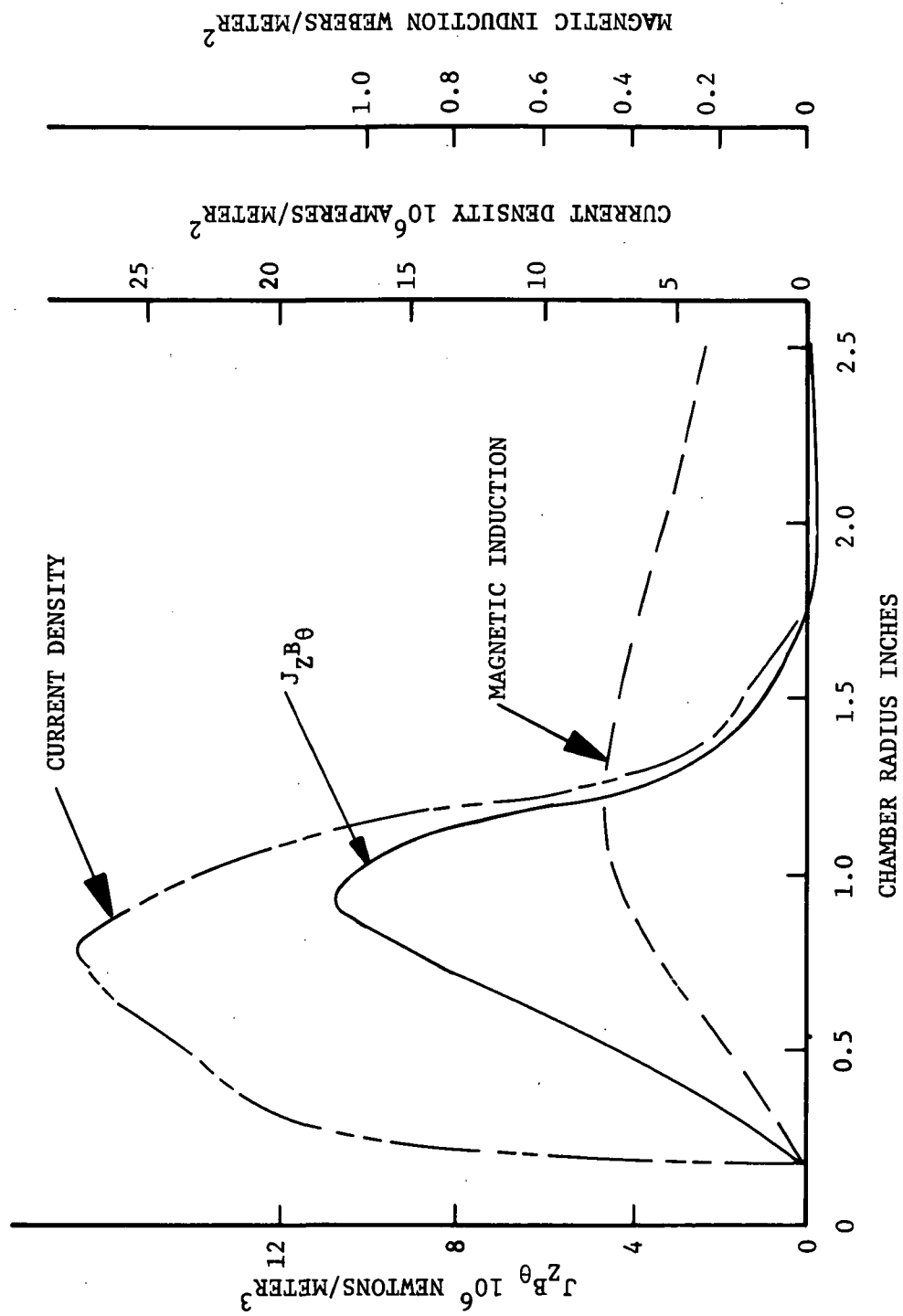


FIGURE 11:  $J_z B_\theta$ , MAGNETIC INDUCTION AND CURRENT DENSITY PROFILES AT  $t = 3.0 \mu\text{sec}$

to be  $3 \times 10^{-17}$  joules per particle, where the radial particle velocity was estimated to be  $3 \times 10^4$  meters/second. For the total entrained mass this corresponds to 36 joules. From Reference 2 for the dynamic pinch phase the energy residing in random translational kinetic energy plus electronic excitation were roughly equal and totalled 0.33 of the radial kinetic energy prior to pinch. Axial kinetic energy of the imploding sheet ions was found in the present study and in (2) to be negligible in comparison to the radial kinetic energy. Thus, the total plasma particle energy of the imploding sheet just prior to pinch was 48 joules. Excluding electronic excitation, the total particle energy was estimated to be 41 joules.

#### 4.3 Plasma Column Formation and Development

Due to the unique ability to identify plasma particle energy and momentum, the axial pressure probe was one of the most important diagnostic tools used in analyzing plasma column behavior. Based on these axial pressure results, three characteristic regions of plasma column behavior prior to total discharge current reversal were noted and analyzed. Identified was a region of intense axial ion (plasma) streaming, followed by regions of plasma column heating and static pressure decay, both evidencing no discernible plasma streaming.

Plasma column axial pressure data presented in Figures 12 and 13 were gathered for the discharge system at negative ground (cathode mounting of pressure probe) and positive ground. Notation regarding probe position follows from Figure 1. Comparison of Figures 12 and 13

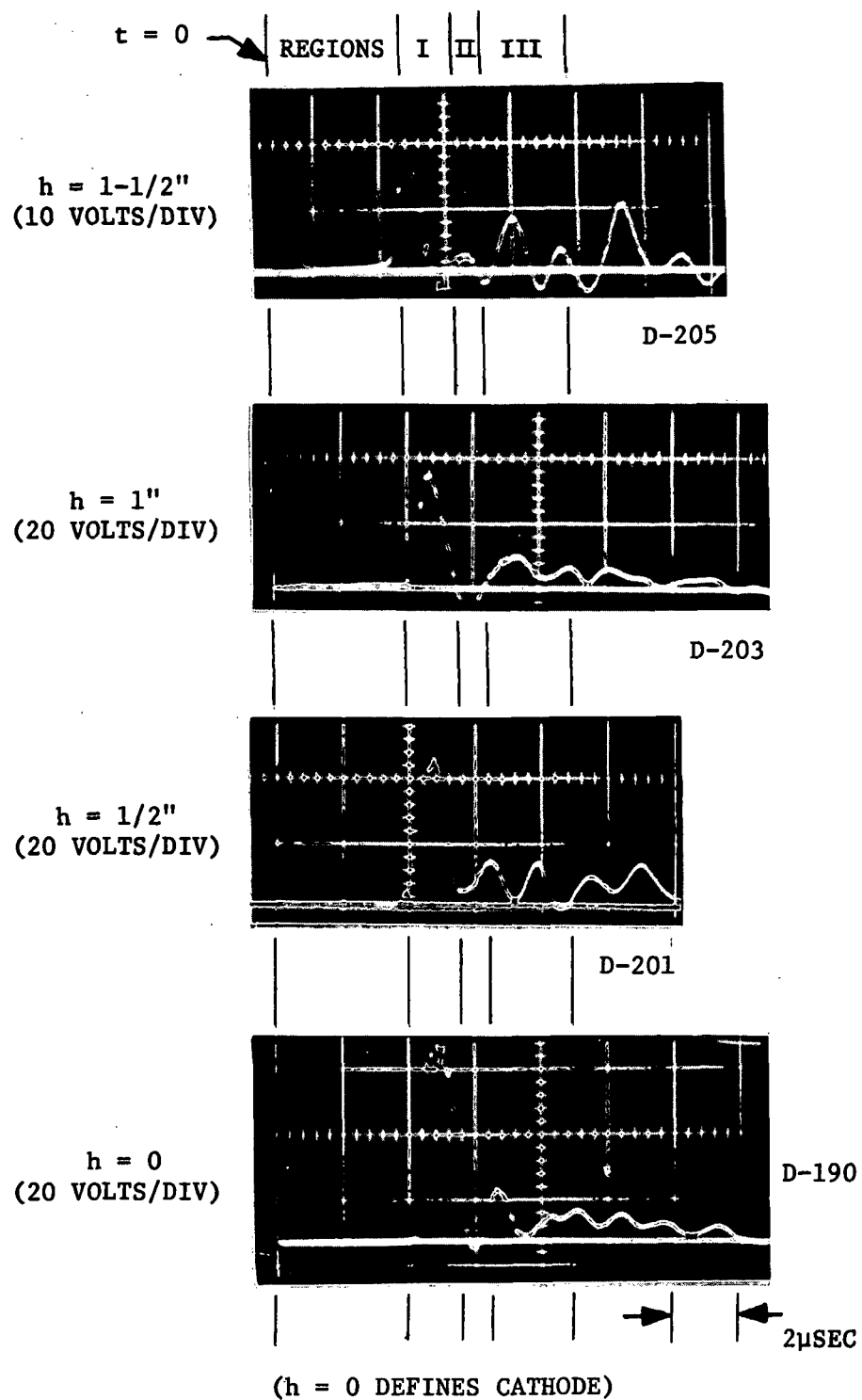


FIGURE 12: PLASMA COLUMN AXIAL PRESSURE RECORDS (NEGATIVE GROUND)

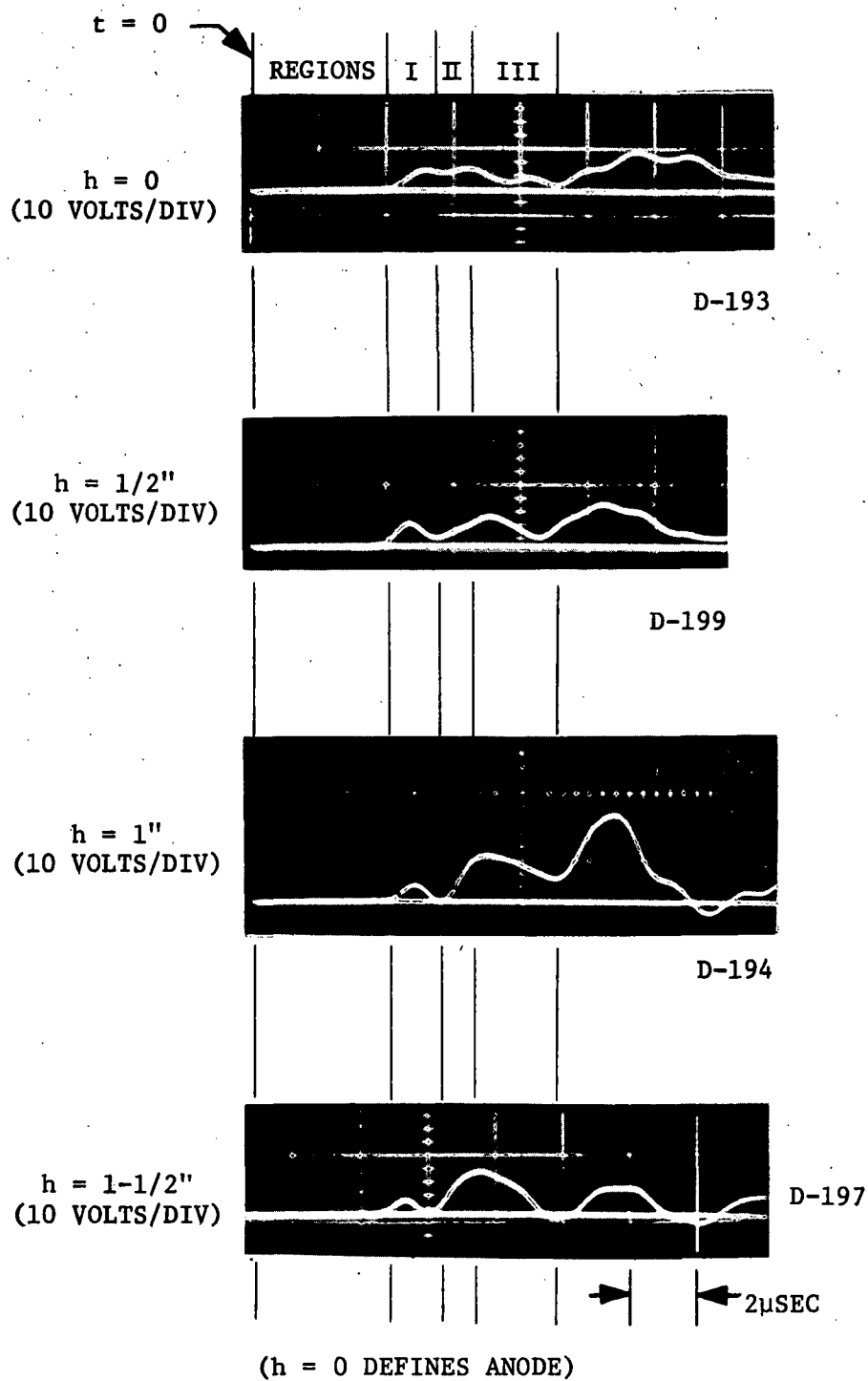


FIGURE 13: PLASMA COLUMN AXIAL PRESSURE RECORDS (POSITIVE GROUND)

reveals a strong pressure asymmetry between  $4.0\mu\text{sec}$  and  $5.5\mu\text{sec}$ , the magnitude depending upon the particular axial station probed. Both the relative polarity of the chamber electrodes and the large difference between electron and ion mass suggest that this asymmetry is a consequence of axial ion streaming. This effect was noted in a detailed experimental analysis of the current sheet (2). The axial variation in magnitude of the pressure asymmetry indicates that the streaming particles are accelerated in the direction of the cathode by some mechanism as they approach the cathode. A consideration of time at axial pressure peak taken from Figure 12 indicates a temporal non-uniformity of the streaming pressure signal along the column axis. Such behavior was not noted for the static pressure (anode mounted) signals. This region of pressure asymmetry will be referred to as region I, indicated in Figures 12 and 13.

For times between  $5.5\mu\text{sec}$  and  $6.5\mu\text{sec}$  the anode and cathode pressure records give no evidence of the pressure asymmetry characterizing region I. Instead, significant heating of the plasma is indicated by the sharp increase in axial static pressure in Figure 12 despite only a slight compression of the column boundary indicated by luminosity. At the chamber midplane static pressures increased by a factor of 4 over the pressure in region I. This regime, characterized by heating, will be referred to as region II.

Considering times greater than  $6.5\mu\text{sec}$ , the static pressure decays until  $t = 9\mu\text{sec}$  after which the plasma from luminosity appears to expand rapidly and make contact with the chamber walls. At midplane

this static pressure decay is small. The region between  $t = 6.5\mu\text{sec}$  and  $9\mu\text{sec}$  will be referred to as region III.

To facilitate analysis, reduced axial pressure results are presented in Figure 14 for axial stations 1/2 inch, 1 inch and 1-1/2 inches referenced to the cathode. These results represent average pressures obtained from two to three discharges conducted under identical conditions. Unless noted otherwise, future specification of axial position will be referenced with respect to the cathode.

#### Region I (Pressure Asymmetry)

Plasma temperature and ion streaming velocity were evaluated from the reduced pressure data. Axial pressure data, noted to vary little across the column, were estimated to be approximately 5 atmospheres. Luminosity indicates that the plasma column expands from approximately 0.2 inch at pinch to 0.4 inches at  $5.5\mu\text{sec}$ , termination of region I. Thus the average column radius was estimated to be approximately 0.3 inches giving a number density of  $1.3 \times 10^{23}$  particles/ $\text{m}^3$ . From the static pressure relation [3.6] the average plasma temperature was then estimated to be

$$T_e + T_i = 2.8 \times 10^5 \text{OK} = 24\text{eV} \quad .$$

The total energy resident in random translational kinetic energy is given by

$$E_r = \frac{3}{2} Nk(T_e + T_i) \quad ,$$

where  $N$  is the total number of particles of a given species in the plasma column. The resultant energy is  $E_r = 7$  joules.

From the impact pressure approximation for the cathode mounted pressure probe, Equation [3.8], the ion streaming velocity  $v_{zi}$  was



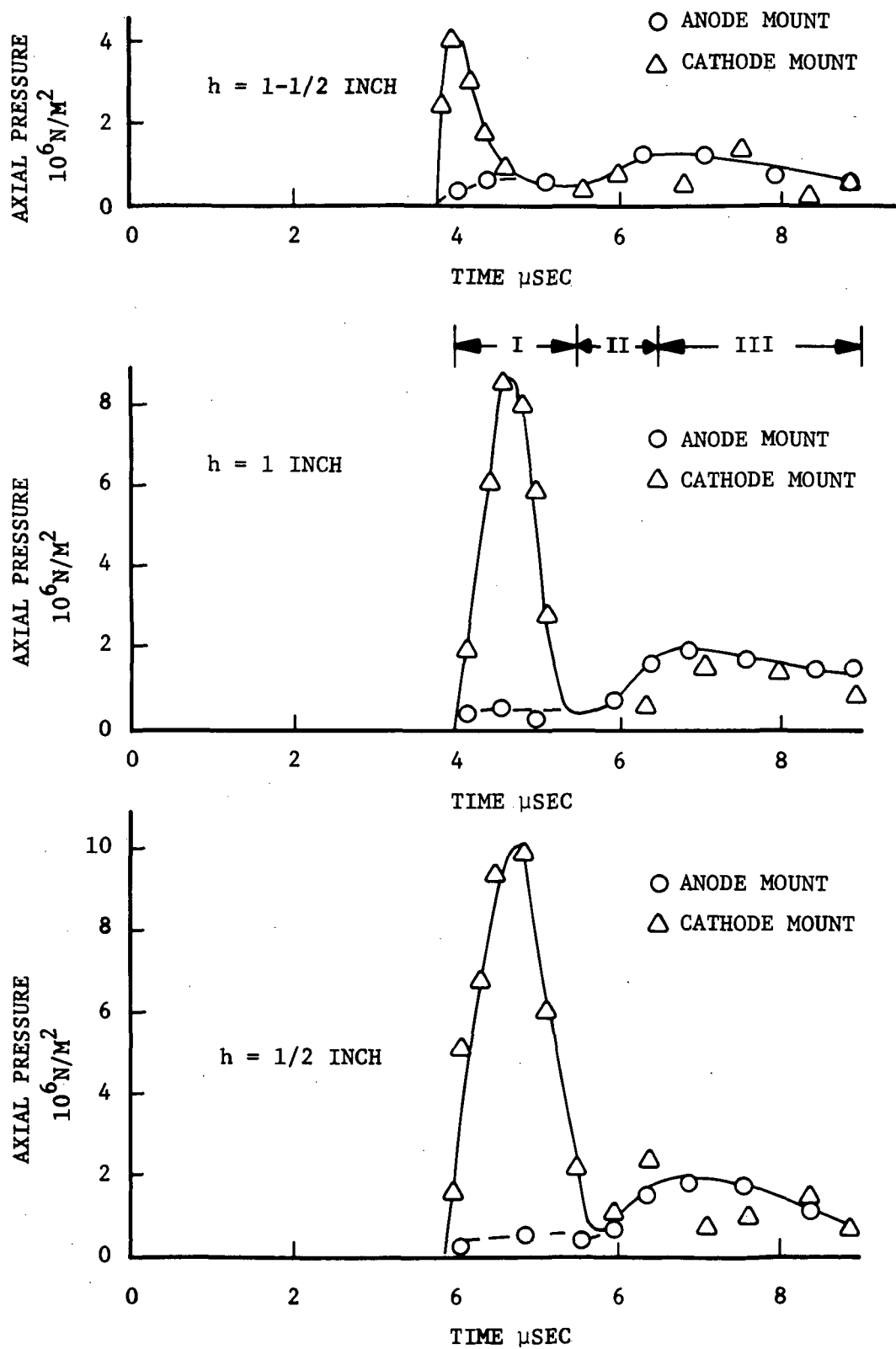


FIGURE 14: REDUCED PLASMA COLUMN AXIAL PRESSURE

estimated on the chamber midplane to be

$$v_{Zi} = 3.2 \times 10^4 \text{ m/sec} ,$$

a value very close to the radial pinch velocity of the imploding current sheet which was estimated to be  $3 \times 10^4 \text{ m/sec}$ . The total axial kinetic energy of the column particles was thus calculated to be 41 joules. When comparing axial streaming kinetic energy and random translational kinetic energy in region I to the prepinch particle energies as presented below, it should be noted that the radial kinetic energy is converted into axial kinetic energy with only slight thermalization of the imploding mass.

	KE axial	KE radial	$E_r$
region I	41 joules	$\sim 0$	7 joules
prepinch	$\sim 0$	36 joules	5 joules

The increase in plasma particle energy between prepinch and region I, 2 joules, is attributed to the continual addition of energy to the discharge from the energy storage capacitor bank.

As a check on the above result, calculation of ion-ion collision time for thermalization of the plasma column was performed using a successive long range coulombic collisional approximation to the collisional process taking place in the plasma column. From Glasstone and Lovberg (16), the expression for ion-ion collision time,  $t_{ii}$ , is for the purpose of an order of magnitude estimate

$$t_{ii} = \frac{4\pi\epsilon_0^2 (2m_i)^{1/2} W_i^{3/2}}{n_i e^4} \frac{1}{\ln \Lambda} , \quad [4.5]$$

where  $W_i$  is ion energy of the scattered particle as it passes through a field of fixed field particles and  $\ln\Lambda$  is the logarithm of the ratio of impact parameter to debeye shielding distance. For the imploding sheet,  $n_i$  was estimated to be  $2 \times 10^{23}$  particles/m<sup>3</sup> from the radial pressure records, and for particle energies of interest,  $\ln\Lambda \approx 6$ . The radial kinetic energy per particle,  $W_i$  based on a  $3 \times 10^4$  m/sec radial velocity at pinch, was found to be  $3.02 \times 10^{-17}$  joules/particle. The collision time was thus estimated to be  $t_{ii} \approx 1 \mu\text{sec}$ , roughly the duration of region I. And so the imploding stream will not be expected to thermalize on the time scale of region I. A more rigorous examination of the collisional dynamics lies outside the scope of this work, but would include the radial kinetic energy of the target ions. This additional consideration would tend to increase ion-ion collision time (16). Thus it can be seen that the plasma column may not have been completely thermalized during region I, but with certainty achieved thermalization at some later time in region II. This fact tends to substantiate the relatively small increase in random translational kinetic energy of the gas noted above. It should also be noted that there will be transfer of energy from the ions to the electrons for the current sheet ion temperature can be expected to be at least as large as the electron temperature. Average ion temperatures postulated in the entrained region of a similar current sheet (2) were found to average approximately 4 to 5 times as great as the electron temperature. This follows by simply considering the relative magnitude in kinetic

energy of overrun ions and electrons as seen by an observer fixed on the current sheet. An estimation of characteristic times for energy transfer from ions to electrons will require a knowledge of the electron temperature in region I, and will now be considered.

Electron temperature was estimated within region I from voltage inner divider data presented in Figure 4 and the classical form of plasma scalar resistivity given by Spitzer (23). The plasma resistance,  $R$ , is given by

$$R = \frac{V_I}{I} .$$

The conductivity of the plasma,  $\sigma$ , equal to the inverse of the resistivity  $\rho$ , is related to current, voltage and plasma column size by

$$\sigma = \frac{LI}{V_I A} , \quad [4.6]$$

where  $A$  is the cross-sectional area of the column and  $L$  is the column height. Presence of the magnetic field which is perpendicular to the axial electric field, in the plasma column requires consideration of the magnetic field in the current conduction process. For that particular case, the conductivity  $\sigma$ , equal to  $\sigma$  from [4.6] is related to the scalar conductivity  $\sigma_o$  by

$$\sigma = \frac{\sigma_o}{1 + \frac{\omega_c^2}{v^2}} , \quad [4.7]$$

where  $\omega_c$  is the electron cyclotron frequency and  $v$  is the total collision frequency of electrons with ions and neutrals. The plasma

is assumed to be 100 percent ionized, therefore, only collisions between electrons and ions will be considered.

From Spitzer, the scalar conductivity can be written as

$$\sigma_o = \frac{1}{\eta} = 3.16 \times 10^{-3} T_e^{3/2} . \quad [4.8]$$

Combining [4.7] and [4.8] and noting that  $\nu = 1/t$  then

$$\sigma = \frac{3.16 \times 10^{-3} T_e^{3/2}}{1 + (\omega_c t_{ei})^2} . \quad [4.9]$$

The cyclotron frequency,  $\omega_c$ , was found for an average magnetic field strength  $B = 0.3$  webers/m<sup>2</sup> across the column cross-section to be  $\omega_c = \frac{qB}{m} = 5.27 \times 10^{10}$  cycles per second. The electron-ion collision time (16),  $t_{ei}$ , is

$$t_{ei} = 2.58 \times 10^{-19} T_e^{3/2} ,$$

where  $n_i \approx 1.3 \times 10^{23}$  particles/m<sup>2</sup> and  $\ln \Lambda = 6$ . The plasma conductivity is thus related to the plasma electron temperature by

$$\sigma = \frac{3.16 \times 10^{-3} T_e^{3/2}}{1 + 1.85 \times 10^{-16} T_e^3} . \quad [4.10]$$

Assuming that the predominant resistive potential drop occurs within the column, where, approximately 21 ka of current flows through a column of radius 0.3 inches, the conductivity from Equation [4.6] becomes  $\sigma \approx 1.2 \times 10^4$  mhos/meter with  $n = 1.3 \times 10^{23}$  particles/m<sup>3</sup> and the

average inner divider voltage roughly 500 volts. Using this value for  $\sigma$  in [4.10] the electron temperature of the column was estimated to be

$$T_{ei} \approx 3\text{eV} ,$$

and was found to be relatively insensitive to the factor of two change in inner divider voltage noted in Figure 4. This electron temperature is in agreement with the value inferred spectroscopically in Reference 22 where the experimental conditions were, as was noted above, close to those for this study. The total kinetic temperature of the plasma was estimated for the present study to be 24 eV, thus the ion temperature in region I is

$$T_{iI} \approx 21 \text{ eV} .$$

This result agrees with the partitioning of kinetic temperature by York (2) and indicates that there was little significant transfer of random thermal kinetic energy between the ions and electrons. An indication of the time scale required for equilibration of electron and ion temperatures was obtained by considering the time for ions and electrons with assumed Maxwellian distributions to equilibrate. From Spitzer (23) where  $\frac{T_e}{m_e} \gg \frac{T_i}{m_i}$  the equilibration time,  $t_{eq}$ , is

$$t_e = \frac{3m_i (k T_e)^{3/2}}{8(2\pi m_e)^{1/2} n_i e^4 \ln \Lambda} . \quad [4.11]$$

Using  $\ln \Lambda$  as before and the electron temperature, 3eV, the equilibration time was estimated to be

$$t_e \approx 0.06 \text{ sec}$$

which is much greater than the duration of region I as well as being much greater than column lifetime. Thus the ions and electrons are essentially thermally independent as experimentally predicted.

Energy can be gained by the electrons directly from the plasma IR drop. Integration of this power input over region I indicates that approximately 15 joules of energy is deposited in the electron population, sufficient to raise the kinetic temperature 52eV if all the energy were deposited in the random translational kinetic energy of the electrons. Loss mechanisms do exist, however, with radiation being the most predominant here (13). The two radiative loss mechanisms are Brehmsstrahlung, which results from the acceleration of electrons in the coulombic fields of the ions and discrete energy level radiation resulting from de-excitation of argon ion electrons excited by the current carrying electron swarm. Kerr cell photographs of the plasma indicate significant energy loss in the visible spectrum.

The power density for Brehmsstrahlung radiation ( $\text{watts/m}^3$ ) is given by (24)

$$Q_{br} = 1.5 \times 10^{-38} n_i n_e T_e^{1/2} .$$

Using the plasma column volume,  $9 \times 10^{-6} \text{ m}^3$ ,  $n_i = 1.3 \times 10^{23} / \text{m}^3$  and  $T_e \approx 3.5 \times 10^4$  the power loss was found to be

$$Q_{br} \approx 3.3 \times 10^5 \text{ watts} .$$

This is at least an order of magnitude lower than the average power ( $IV_I$ ) and is thus negligible source of energy loss.

The power loss by electronic excitation of argon ions by inelastic encounters with the electron stream appears to be the major electron energy loss mechanism in the column. From (13) the power loss per unit volume of plasma due to excitation is given for excitation in each argon atom-electron collision by

$$Q_e = n_e X t_{ex}^{-1} ,$$

where  $X$  is the excitation energy and  $t_{ex}$  is time to excite an argon atom. For the plasma parameters,  $n$ ,  $T_e$  given above and  $X = 11.5$  eV the power loss by inelastic collision was found to be

$$Q_e \approx 5 \times 10^6 \text{ watts} .$$

This is approximately the same magnitude as  $IV_I \approx 10^7$  watts. For the plasma column the gas is assumed to be at least singly ionized thus  $t_{ex}$  and  $X$  would have to be adjusted for the argon ion. The adjustment apparently is not significant, however, for it is the only loss mechanism which appears to be great enough in magnitude to explain the constancy of  $T_e$ . The total energy balance for the discharge chamber based on total voltage, indicates that over one-half of the system energy was lost by radiation thus further strengthening the dominance of the electron-ion excitation loss mechanism.

The detailed total energy balance within the discharge chamber will now be considered in an effort to further clarify system energy losses and energy deposition. Energy deposited in the discharge chamber is resident in many different modes. The most general energy modes are



thermal energy or internal energy, streaming kinetic energy and magnetic field energy. The sum of these energy modes must be equal to the total energy deposited within the discharge chamber,  $E_{\text{total}}$ , which was found by integrating  $IV_c$  over time

$$E_{\text{total}} = \int_0^t IV_c dt \quad .$$

This integral was evaluated using data from Figures 2 and 4 and is presented in Figure 15. The total energy,  $E_{\text{total}}$ , was found to increase from 145 joules at  $t = 4\mu\text{sec}$  to 200 joules at  $t = 5.5\mu\text{sec}$  indicating a significant increase in energy transfer to the discharge chamber. The thermal energy modes which include random translational energy,  $E_r$ , ionization energy,  $E_{\text{ion}}$ , electronic excitation energy,  $E_{\text{excite}}$ , and radiation,  $E_{\text{rad}}$ , will be analyzed first. A discussion on the energy which is resident in ion streaming kinetic energy and magnetic field will then follow. As mentioned above the thermal energy of the plasma,  $E_t$  will be equal to the sum

$$E_t = E_r + E_{\text{ion}} + E_{\text{excite}} + E_{\text{rad}} \quad .$$

The random thermal energy was evaluated earlier

$$E_r = \frac{3}{2} Nk (T_e + T_i) \approx 7 \text{ joules} \quad .$$

The energy required for 100 percent single level ionization using

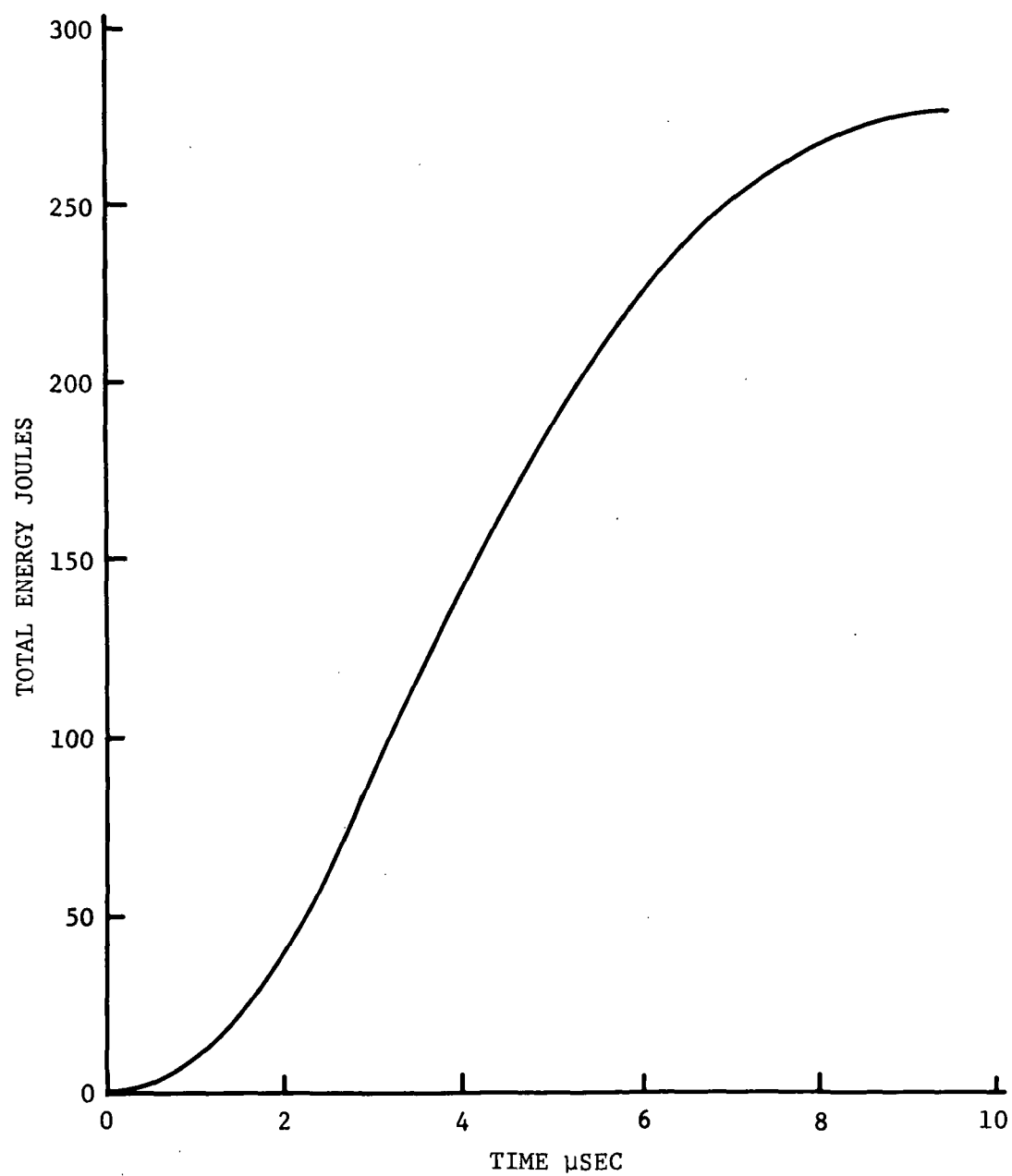


FIGURE 15: DISCHARGE CHAMBER TOTAL ENERGY

$2.52 \times 10^{-18}$  joules per particle ionization energy is

$$E_{\text{ion}} \approx 3 \text{ joules} .$$

Following York (2), electronic excitation energy was estimated from the results obtained by Knoche (25) who considered the thermodynamic properties of argon for temperatures up to  $10^5 \text{ K}$ . For equilibrium between random translational energy states and electronic excitation energy states, dominant 6th and 7th level ionization were predicted. Spectroscopic results presented in (19), however, indicate that the ionization level should be predominately 1st and 2nd level thus the random translational states and electronic excitation states are not in complete equilibrium. Considering 1st and 2nd level ionization, the nonequilibrium temperature for electronic excitation was estimated from which the energy resident was found to be

$$E_{\text{el}} \approx 4 \text{ joules} .$$

The remaining thermal energy term, the energy loss by radiation, will be inferred from the total energy deposited and the sum of all other energy components

$$E_t = 14 + E_{\text{rad}} \text{ (joules)} .$$

The magnetic field energy was estimated by integrating the magnetic energy density within the discharge chamber. The coaxial design of the discharge chamber essentially precludes discharge magnetic field

from leaking outside the chamber. Thus

$$E_{B_\theta} = \int_0^{r_c} \frac{B_\theta^2}{2\mu_0} 2\pi r h dr ,$$

where  $r_c$  is the radius of the discharge chamber return outer conductor. Magnetic field energy was found to increase slightly in region I from 25 joules at 4.0 $\mu$ sec to 30 joules at 5.5 $\mu$ sec. The average magnetic field energy 28 joules was considered representative of the magnetic field energy stored in region I.

The axial streaming kinetic energy,  $E_{ke}$ , was estimated from the inferred discharge chamber midplane axial velocity measurement  $v_{zi} \approx 3.2 \times 10^4$  meters/sec and found to be

$$E_{ke} \approx \frac{1}{2} N m_i v_{zi}^2 \approx 41 \text{ joules} .$$

Thus knowing  $E_t = 14 + E_{rad}$ ,  $E_{B_\theta}$ ,  $E_{ke}$  and  $E_{ion}$  the radiation energy loss was found to vary almost linearly with time from

$$\begin{aligned} E_{rad} &\approx 71 \text{ joules at } t = 4.0\mu\text{sec} \\ \text{to } E_{rad} &\approx 121 \text{ joules at } t = 5.5\mu\text{sec} . \end{aligned}$$

Thus at least one-half of the energy deposited within the discharge chamber is resident in radiation. The difference in energy loss by radiation in region I was found from above to be in good agreement

with the net energy gain from the voltage inner divider measurement

$$E_I = \int_{4\mu\text{sec}}^{5.5\mu\text{sec}} IV_I dt \approx 45 \text{ joules} .$$

This implies, as was noted before, that the power lost by radiation appears to be balanced by the power delivered to the current carrying electrons.

From the above energy analysis, it can be seen that over 50 percent of the discharge chamber energy not lost by radiation is resident in axial streaming kinetic energy. This streaming is characteristic of region I and was found to be one order of magnitude greater than the axial streaming velocity observed by York (2) ( $3 \times 10^3 \text{ m/sec}$ ) in a thin current sheet at chamber half radius,  $r = 2$  inches. The pressure asymmetry in the current sheet was related to sheet tilt angle (2). Axial pressure data were also taken in the present study at  $r = 1/2$  inches to ascertain plasma streaming. This off centerline axial data was taken at a slightly higher chamber initial fill pressure but the inferred axial streaming velocity was adjusted to 70 $\mu$  initial fill pressure. The region of predominant ion streaming was estimated to have a  $1/2$  inch width at the  $1/2$  inch radius chamber station and had a pressure asymmetry of about 1 atmosphere. The streaming velocity  $v_{Z1 \ 1/2}$  was thus estimated to be

$$v_{Z1 \ 1/2} = 7 \times 10^3 \text{ m/sec} .$$

This is  $1/5$  of pinch streaming estimated earlier to be  $3.2 \times 10^4$  m/sec, thus indicating the presence of an acceleration mechanism of significant magnitude acting on the ions during the last  $1/2$  inch of pinch. The plasma column radius was 0.3 inches implying that the mechanism for this rapid increase in velocity is associated with the formation of the plasma column.

The existence of axial streaming in the pinched plasma column has received some consideration within the past 15 years (3, 26, 27, 28, 29). Experimental investigations conducted with such devices indicated significant neutron production after the plasma was compressed into the highly energetic plasma column. The theoretical models proposed for neutron production have hypothesized plasma axial acceleration mechanisms within the pinched column for rationalizing this neutron behavior. However, the existence of axial plasma acceleration or streaming has not been directly verified in any of these experimental investigations due to the lack of an adequate sensor. In the present investigation, a piezoelectric pressure transducer of proven past performance in a plasma environment (17) was used to axially probe the pinched plasma column. Energetic ion streaming was clearly observed in the present investigation, as noted above, and a consideration of possible mechanisms for such behavior as outlined in these earlier efforts will now be considered.

Anderson, et al., (3) first proposed in 1958 that electric fields generated by the growth of  $m^1 = 0$  "sausage" type instabilities was

responsible for accelerating deuterons to energies great enough for neutron production. Axially propagating luminous fronts were noted by Folkierski, et al., (26) from Kerr cell photographs of the plasma column. These axial fronts referred to as "shocks" by the author, followed axial contraction ( $m' = 0$  instabilities) observed in the regions of the electrodes.

Pert (27) in 1969 proposed a model for rationalizing the experimentally observed axial velocity of plasma passing through the exit plane of a conical Z-pinch device. Calculation of the plasma velocity was based on a combination snowplow - gas dynamic nozzle model.

The existence of axial streaming of ions in the plasma focus and Z-pinch has been discussed recently in the literature by Bernstein (28) and (29) as a possible mechanism for neutron production observed in pinched plasma columns. Two models were considered by Bernstein which may be applicable here. The first model (28) follows from the hypothesized axial expansion of plasma along the column centerline resulting from nonsimultaneous pinching of the plasma column. Current sheet tilt prior to pinch was noted in the present study as well as a nonsimultaneous record of axial streaming pressure along the plasma column centerline. The second model (29) proposed by Bernstein results from the unimpeded acceleration of individual ions in the  $E_z$  and  $B_\theta$  fields resulting from rapid contraction of the plasma boundary. This model has apparently accounted for the measured characteristics of the neutrons produced in the plasma focus. Each of the above models were considered potential driving mechanisms for the pressure asymmetry

observed and thus investigated in more detail. They will now be considered in chronological order.

The  $m' = 0$  MHD instability was proposed by Anderson et al. as a mechanism for axial plasma acceleration in the Z-pinch device. The accelerating mechanism is based upon axial electric fields induced by the time varying flux or time varying inductance across the highly necked regions of the instability. Anderson calculated the potential generated across one lobe of the sausage shaped instability by evaluating the rate of change in inductance of the constriction,

$$V = I \frac{dL}{dt} \quad [4.12]$$

Examination of the voltage records for the present experiment (Figure 4), between  $4\mu\text{sec}$  and  $4.5\mu\text{sec}$  where axial streaming pressure peaks, indicates that there was essentially no inductive voltage drop across the column. The voltage drop was essentially resistive. For  $t > 4.5\mu\text{sec}$  a noticeable difference in the voltage records was noted but this occurs after the axial pressure asymmetry begins to fall. Kerr cell photographs give no indication of current shorting on the outer wall of the discharge chamber, thus the voltage from [4.12] would have to appear on the voltage records. Had shorting been noted, however, the voltage drop associated with [4.12] would not be seen on the voltage records. Furthermore, visual examination of the Kerr cell records does not give any indication of the  $m' = 0$  instability of the electrodes as noted by Folkierski (26) in argon or at any other axial cross-section of the plasma column. Thus based on voltage and Kerr cell records the  $m' = 0$  instability does not



appear to exist at any station along the plasma column during axial ion streaming and thus is not considered a mechanism for ion streaming in this experiment.

A nonsimultaneous pinching model was proposed by Pert (27) to describe the observed axial motion of a plasma element propagating through the exit plane of a conical Z-pinch device. Current sheet tilt, a necessary condition for the applicability of such a model to the present study was estimated in the present case from the axial  $\dot{B}_\theta$  time to half peak trajectory at  $r = 1/2$  inch. The tilt angle was found to be 14 degrees thus predicting nonsimultaneous pinch, consistent with Pert's conical pinch model. Pert describes the motion of the plasma element partly by the electromagnetic acceleration (radial and axial) produced by the discharge and partly by the ejection of plasma particles from the pinch formed central column. The average axial velocity of the plasma passing through the exit plane was based upon the momentum average of the above components. The calculated momentum described by the electromagnetic acceleration process, the axial pinch point momentum in particular, was based upon a conical geometry variation of the original snowplow model (21). This component of momentum was then averaged with the momentum of gas ejected axially from the column using a choked nozzle flow approximation in which the gas leaves the column at the speed of sound,  $v_t$

$$v_t = \left( \frac{\gamma k T}{m_i} \right)^{1/2} .$$

For the present study  $v_t$  was estimated to be  $2.2 \times 10^3$  m/sec with  $T \approx 24$  eV and  $\gamma = 1.2$ .

The axial pinch point velocity,  $v_p$ , can be estimated from the radial velocity of the current sheet ( $3 \times 10^4$  m/sec) and the tilt angle (14 degrees) at  $r = 1/2$  inch. The pinch point velocity was estimated to be  $7.2 \times 10^3$  m/sec for the above conditions. Thus the average momentum velocity would lie between  $2.2 \times 10^3$  m/sec and  $7.2 \times 10^3$  m/sec in the present case. In order to fix the average mass velocity, the mass accelerated by electromagnetic means and mass flow through the sonic nozzle must be found. The mass accelerated by the electromagnetic forces into the pinched column extending to the discharge chamber mid-plane, is approximately 40 percent total chamber or  $4 \times 10^{-8}$  kilograms. The mass flux through the column axial cross-section is given by (27)

$$M_t = m_i \delta t n A \left[ \left( \frac{kT_i}{m_i} \right) \gamma \left( \frac{2}{\gamma+1} \right)^{\gamma+1/\gamma-1} \right]^{1/2},$$

where  $\delta t$  is the plasma element time of formation, approximately  $0.4 \mu\text{sec}$ . Using the appropriate input values  $M_t$  was found to be  $8.5 \times 10^{-12}$  kg. The mass accelerated by the electromagnetic forces is therefore much greater than the sonic mass flow thus the average mass velocity,  $v$ , is given by

$$v \approx v_p \approx 7.2 \times 10^3 \text{ m/sec}.$$

As a result the gas velocity corresponds to the axial pinch point velocity. This result differs from the experimentally determined value  $3.2 \times 10^4$  m/sec by almost a factor of 5. It should be remembered however that  $v_p$  was estimated at  $r = 1/2$  inches rather than at  $r = 0$ , thus if the current sheet tilt angle increased significantly over the remaining  $1/2$  inch of current sheet implosion, then  $v_p$  would also show a significant increase. Assuming that the current sheet tilt angle was doubled at pinch, 28 degrees, then  $v_p = 1.4 \times 10^4$  m/sec and the streaming velocity is then only a factor of 2 less than the experimentally determined ion streaming velocity.

The nonsimultaneous pinching model by Bernstein (28) will now be considered. Using a simple fluid model, Bernstein assumed that the work done in the axial expansion of a cylindrical plasma is equal to the increase in axial kinetic energy of the expanding plasma. Thus

$$- \int_0^t \frac{\partial P}{\partial Z} \frac{\partial Z}{\partial t} dt = \frac{1}{2} \frac{d}{dt} \int_0^L n_i m_i \left( \frac{dZ}{dt} \right)^2 dZ ,$$

where  $P$  is the plasma static pressure and  $L$  is the length of the expanding plasma. Pinch occurs first on the anode based on the observed current sheet tilt implying gas expansion toward the cathode. Thus in this respect, Bernstein's model (28) and the experimental pressure results are in agreement. Assuming a spatially constant temperature with decreasing density and pressure across  $L$  and furthermore assuming that the density profile is constant in time, the axial velocity,  $v_{Zi}$ ,

assumed to increase linearly across the column length from rest is

$$v_{Zi} \approx \frac{12kT_i \Delta t}{m_i L} \quad [4.13]$$

Substituting into [4.13] the observed column ion temperature,  $T_i = 2.44 \times 10^5 \text{°K}$ , and the observed difference in arrival time  $\Delta t$  for acceleration to the midplane,  $0.4 \mu\text{sec}$ , the axial velocity was estimated to be

$$v_{Zi} \approx 1.0 \times 10^4 \text{ m/sec}$$

This result is roughly a factor of 3 lower than the experimentally observed axial velocity at midplane. The observed axial plasma velocity was found to increase along the axis toward the cathode but with a rate greater than linear as suggested by the model. Static pressure records indicate that plasma static pressure does not vary significantly across the column length in contrast to the assumed linearly decreasing variation in both pressure and density. This apparent discrepancy can be relaxed however due to the constant addition of mass along the axis brought about by continuing nonsimultaneous pinching of the current sheet. It should also be noted that the factor of 3 discrepancy in axial velocity may be accounted for by additional heating of the plasma ions from additional  $\vec{J} \times \vec{B}$  constriction of the plasma mass behind the expanding plasma. Thus the above described gas dynamic expansion model must be considered in light of the assumptions as a probable mechanism contributing to axial ion streaming.

Bernstein's alternate model (29) suggests the existence of deuterons accelerated in intense electric and magnetic fields created by a tightly

constricting plasma column. Bernstein proposed that the annular current sheet of a linear Z-pinch device makes a transition to a columnar distribution with a linear current density highly peaked on the chamber axis. This boundary collapses, enclosing the entire circuit current, and was found by Bernstein to generate axial electric fields high enough to result in orbital deuteron velocities of sufficient magnitude for neutron production. Time averaged deuteron axial velocities upon which the orbital motion can be considered to be superimposed were found to be very high, on the order of  $10^6$  m/sec for a 700 ka discharge (29). Total orbital velocities however were found to be 2 to 3 times as great.

Collapsing of the plasma column, of fixed total current, with time will induce an axial electric field,  $E_z$ , as a result of the rate of increase in magnetic field,  $B_\theta$ , by Faradays Law,

$$\frac{\partial E_z}{\partial r} = \frac{\partial B_\theta}{\partial t} \quad [4.14]$$

The magnetic field  $B_\theta$  was evaluated from Amperes' law,

$$J_z = \frac{1}{\mu_0 r} \frac{\partial(rB_\theta)}{\partial r} \quad [4.15]$$

Note that time dependent constriction of the column boundary effectively increases current density, thus making  $\dot{B}_\theta$  time dependent. Bernstein considered motion in two dimensions,  $r - z$  plane, between ion-ion collisions. The equations of motion used were

$$m_i \ddot{r} = -e \dot{z} B_\theta \quad [4.16]$$

and

$$m_i \ddot{z} = e \dot{r} B_\theta + e E_z \quad [4.17]$$

where

$$B_\theta = B_\theta(r, t), \quad E_z = E_z(r, t) \quad .$$

Coordinate directions were obtained from the right hand rule defined by the vector crossproduct  $\vec{e}_r \times \vec{e}_\theta = \vec{e}_z$  where  $\vec{e}$  denotes the unit vector.

Argon ion trajectories were calculated by simultaneously solving the trajectory equations [4.16] and [4.17] using a time interval iteration scheme. Knowing the total current flowing within the plasma column and using the linear current density approximation, the current density profiles were generated. Integration of expressions [4.14] and [4.15] along with electric field inferred from the voltage inner divider data enabled calculation of  $E_z$  and  $B_\theta$  for use in [4.16] and [4.17]. The most probable particle speed  $C_{mp}$  was selected as the initial speed for all trajectory calculations.

$$C_{mp} = \left( \frac{2kT}{m_i} \right)^{1/2} \quad .$$

For the ion static temperature, 21eV, the most probable speed was found to be  $C_{mp} = 10^4$  m/sec.

Numerical calculations were carried out, starting at this initial velocity, over a time interval corresponding to the time between ion-ion collisions. This time interval was estimated from [4.5], where, for this particular case, the collision energy,  $W_i$ , corresponds to the

ion thermal energy. Based on the ion temperature obtained earlier, 21eV, the collision time was estimated to be 0.1μsec. Due to the presence of strong magnetic fields the possibility of many cyclotron revolutions of the ions over the 0.1μsec acceleration time interval must be considered in order to pick an acceptable iteration time interval. Bernstein found in his investigations that the ion completed many cyclotron revolutions between collisions. Considering acceleration from the plasma column boundary, chosen to be approximately 5 mm, the cyclotron frequency was found to be

$$\omega_c = \frac{qB}{m} = 10^6 \text{ cycles/second} .$$

The magnetic field strength used here was 0.5 webers/m<sup>2</sup> on the boundary. Thus the ion may complete one cyclotron orbit in 1μsec, a time much longer than the acceleration time. Accordingly, the integration interval was chosen to be 0.02μsec.

Trajectories were analyzed for three different initial conditions, they were: (1) positive radial velocity of the ion on the column boundary (2) negative radial velocity of the ion on the boundary and (3) negative radial velocity of the ion on the chamber centerline. In each case the ion was considered to have initially a positive axial velocity component of  $5.8 \times 10^3$  m/sec with a radial component  $\pm 5.8 \times 10^3$  m/sec, the sign depending upon the particular case considered. Electric field strengths were calculated from [4.14] and found to rise linearly in essence from 0 on axis to approximately 800 volts/meter on the boundary. Electric field strengths estimated from voltage inner divider measurements

indicate a peak field strength of  $1.24 \times 10^4$  volts/meter which then drops to 5000 volts/meter or at  $t = 5.5\mu\text{sec}$ . Thus it can be seen that the magnetic induction contribution to the axial electric field strength is small at  $t = 4\mu\text{sec}$  and becomes increasingly more important as  $t \rightarrow 5.5\mu\text{sec}$ . This can be seen from the voltage data in Figure 4. For this study the voltage peak was considered, time between  $4\mu\text{sec}$  and  $4.5\mu\text{sec}$ , also corresponding to peak recorded axial streaming pressure.

Considering the  $0.1\mu\text{sec}$  acceleration time limit the following increases in ion axial velocity were obtained:

- Case 1       $3.7 \times 10^3 \text{ m/sec}$
- Case 2       $2.26 \times 10^3 \text{ m/sec}$
- Case 3       $3.12 \times 10^3 \text{ m/sec.}$

Thus it can be seen that ions on or very near the discharge chamber axis will experience the greatest ion axial accelerations. The order of magnitude difference between case 1,  $3.7 \times 10^3 \text{ m/sec}$ , and the experimentally measured ion streaming velocity,  $3.2 \times 10^4 \text{ m/sec}$  should be noted. However, the calculated acceleration time of  $0.1\mu\text{sec}$  may be in error by as great a factor as 2 or more (16), accordingly changing the calculated velocity.

Based on the results of the models presented above, the probable mechanism for the observed axial streaming of the ions is an axial pressure gradient introduced along the discharge chamber axis resulting from the nonsimultaneous pinching of the column. This nonsimultaneous



pinching results from the current sheet tilt observed in this study and elsewhere (2).

### Region II

The time interval defining region II, 5.5 $\mu$ sec to 6.5 $\mu$ sec, has several definable features some of which have been noted above. Static pressures obtained from axial probing of the plasma column were determined to increase by a factor of 4 at positions probed, except 1/2 inch from the anode where a factor of 2 rise was noted. The pressure asymmetry characterizing region I was found to be nonexistent in region II. This suggests the existence of an energy transfer mechanism or mechanisms through which the axial streaming kinetic energy of region I is transferred into random translational kinetic energy of region II. Such a possibility will be discussed. It will first be noted that photographs of luminosity indicate a slight column contraction, with the midplane diameter decreasing from 0.8 inches at 5.5 $\mu$ sec to 0.7 inches at 6.5 $\mu$ sec. The plasma column volume was thus taken to be a constant value for data analysis.

Using a time averaged plasma column diameter of 0.75 inches, the plasma column number density was calculated from the number of single species particles swept up,  $1.2 \times 10^{18}$  particles, the same value used in region I. Thus in assuming no net gain or loss of plasma

$$n_{II} \approx 1.9 \times 10^{23} \text{ particles/m}^3$$

Using the perfect gas law (3-6), the change in total plasma static

temperature was estimated to be

$$\Delta T_{II} \approx \frac{\Delta p}{n_{II} k} \approx 50 \text{ eV} .$$

This corresponds to an increase in random translational kinetic energy

$$\Delta E_r = \frac{3}{2} N k \Delta T_{II} \approx 14 \text{ joules} .$$

This increase in random translational kinetic energy, 14 joules, is noted to be 0.33 the peak axial streaming kinetic energy, 41 joules, resident in region II. Thus  $\Delta E_r$  does not account for all of the streaming kinetic energy observed in region I. An attempt will be made here to account qualitatively for the rapid increase in random translational kinetic energy,  $\Delta E_r$ , in region II.

Consideration was first given to heating of the plasma column due to viscous dissipation and axial compression within the plasma column. This problem has been investigated by Toepfer et al. (30) for a dense plasma focus. Consideration was given to an ion energy balance equation where Brehmsstrahlung radiation losses and energy transfer between the electrons and ions were considered small in comparison to the effects of compression and viscosity. Radial gradients in the axial streaming velocity were estimated to be at least an order of magnitude greater than the axial gradients in the present experiment. Thus the compressive heating term was found to be small in comparison to the viscous dissipation term. The ion energy equation from (30) then simplifies to a balance between the rate of increase in random translational kinetic

energy of the ions to the viscous dissipation arising from the radial gradient in the axial streaming velocity,

$$\frac{\partial}{\partial t} (kT_i) \approx \left( \frac{m_i}{2\pi} \right)^{1/2} \frac{(\gamma-1)}{n_i e^4 \ln \Lambda} \left( \frac{\partial v_{zi}}{\partial r} \right)^2 (kT_i)^{5/2} .$$

Integrating this expression, the ion temperature was found as a function of time to be

$$\frac{T_i}{T_{i0}} \approx \frac{1}{\left\{ 1 - \left[ 1.57 \left( \frac{m_i}{2\pi} \right)^{1/2} \frac{(\gamma-1)}{n_i e^4 \ln \Lambda} \left( \frac{\partial v_{zi}}{\partial r} \right)^2 (kT_{i0})^{3/2} \right] t \right\}^{2/3}} . \quad [4.18]$$

where  $T_{i0}$  is the initial ion temperature. Considering heating to take place from  $t = 4.0 \mu\text{sec}$ , where ion streaming begins to become pronounced, to  $6.5 \mu\text{sec}$ , where temperature peaks, then from [4.18] where  $T_{i0} \approx 21 \text{eV}$

$$\frac{T_i}{T_{i0}} \approx 1.4 .$$

The radial velocity gradient,  $\partial v_{zi}/\partial r$ , was considered to be a constant and was evaluated by considering the streaming velocity to decrease from its peak value on axis to zero on the column boundary. Therefore, on the basis of such an analysis, it can be shown that approximately 20 percent of the increase in random translational kinetic energy would result from viscous dissipation.

Another potential source of plasma heating arises from the excitation of wave instabilities within the plasma resulting from the passage of high electron currents (31). Theoretical and experimental investigations of excitation of wave instabilities resulting from the passage of high currents have been conducted (31, 32, 33). The resulting heating of the plasma was observed in these cases and was accompanied by an anomalous resistance across the length of the plasma column. Two basic current carrying instabilities were discussed (32, 33); they were the ion-acoustic instability and the "Bunemann" instability. Excitation of the ion-acoustic instability follows from the generation of growing ion-acoustic waves by the flow of electron current where the electron current velocity,  $v_e$ , and species temperatures must satisfy the conditions (31, 33)

$$v_e > \left[ \frac{kT_e}{m_i} \right]^{1/2} \text{ and } T_e \gg T_i . \quad [4.19]$$

The condition  $T_e \gg T_i$  was satisfied in the experimental investigations (32, 33) but was violated in the present study. In the case of the "Bunemann" instability the electron current velocity must be greater than the thermal velocity of the electrons for excitation. Thus for excitation of the "Bunemann" instability (32, 33)

$$v_e > \left[ \frac{kT_e}{m_e} \right]^{1/2} . \quad [4.20]$$

Satisfaction of the instability conditions [4.19] and [4.20] was checked using the electron temperature, determined above to be 3ev, and

the current carrying electron velocity evaluated from

$$J = J_e \approx n_e e v_e .$$

Excitation of the ion-acoustic instability was found to be marginally possible with  $v_e \approx 6 \times 10^3$  m/sec and  $\sqrt{kT_e/m_i} = 3.8 \times 10^3$  m/sec. The electron thermal velocity was found to be approximately  $10^6$  m/sec thus the "Bunemann" instability was not excited in accordance with [4.20].

Examination of the inner divider voltage records identifies no sharp rise in plasma resistivity in region II contrary to experimental findings and predictions (31, 32, 33). In fact in the present study, a slight drop in inner divider voltage was observed in region II. Due to the fact that  $T_i > T_e$  in the present study consideration of  $T_i$  in place of  $T_e$  in [4.19] may be more appropriate if indeed the plasma could support unstable ion-acoustic waves under this species temperature condition. Using  $T_i$  in place of  $T_e$  the following result was obtained.

$$\left[ \frac{kT_i}{m_i} \right]^{1/2} \approx 10 \times 10^3 \text{ m/sec}$$

As a result, the basic expression [4.19] is not satisfied. It should be noted however that  $v_e$  was based on an average current density,  $J$ , for the plasma column. This average would be much less than the  $J$  values near the axis. In the present study the current density on the axis was estimated to be 4 to 5 times as great as the average value based on a linear rise in  $J$  within the column. This is not great enough however to satisfy the "Bunemann" condition however but may be sufficient to

excite the ion-acoustic instability. Thus the existence of the ion-acoustic instability as a mechanism for heating the plasma in region II appears uncertain. Furthermore it should be noted that in the experimental investigations reported here (32, 33) the plasma column number density was on the order of  $10^{18}$  to  $10^{19}$  particles/m<sup>3</sup>, 4 to 5 orders of magnitude less than the plasma column number densities in the present study. Although number density does not appear explicitly in the instability conditions [4.19] and [4.20], their applicability to the present investigation is uncertain.

Examination of Figure 15 indicates that the energy added to the discharge chamber in region II is clearly sufficient to account for the energy addition postulated, however, the responsible mechanism or mechanisms remains to be clarified.

### Region III

A region of static pressure decay within the plasma column following region II but prior to termination of plasma column life was identified. As in region II there was no evidence of axial pressure asymmetry which characterized region I. Luminosity photographs show a loss of plasma column definition as compared to that noted in regions I and II. A midplane oscillatory behavior of the boundary was also noted.

For the above stated reasons, specification of plasma column volume in regions III was more difficult than for the other two regions. Nonuniform boundary diameter prompted calculation of column volume based on a diameter obtained from an average of the electrode and midplane

values. An effective average column diameter of 0.9 inches was used with the assumption of no radial loss of plasma to the walls to allow estimation of column number density,  $n_{III} \approx 1.1 \times 10^{23}$  particles/m<sup>3</sup>. Total plasma temperature was then estimated from (3-6) using an average static pressure of 17 atmospheres to be,  $T_{III} \approx 10.8 \times 10^5$ °K. The random translational kinetic energy of the plasma was then estimated to be  $E_r \approx 26$  joules in region III, an increase of approximately 6 joules over the average of region II. Thus, region III is also a region of plasma heating although not as intense as region II where an energy change due to thermalization of 14 joules was noted.

In summary, the plasma particle energies,  $E_p$ , streaming kinetic energy plus random kinetic energy for each of the definable regions are listed below along with the total average energy deposited within the discharge chamber,  $E_{total}$ , at the time of estimation:

Region	$E_p$ (joules)	$E_{total}$ (joules)
I	48	180
II	21	220
III	26	260

It can be seen that in region I the largest percentage of discharge chamber energy is resident within the plasma, 25 percent, with over 80 percent of this plasma energy resident in plasma streaming. Although magnetic field energy does increase by almost 20 joules from 28 joules in passing from region I to region III, the energy loss due to radiation

clearly dominates the discharge chamber energy balance in all regions as can be deduced from the tabulated results above. Approximately 50 percent of the energy deposited within the discharge chamber in regions I was found to be lost by radiation. This radiation loss was estimated to increase to over 70 percent of discharge chamber energy in regions II and III. Considering the total capacitor bank storage energy,  $2.5 \times 10^3$  joules, the plasma particle energy in region I comprises approximately 2 percent of this bank energy.



## CHAPTER V

## SUMMARY AND CONCLUSIONS

Several plasma diagnostic techniques were applied for investigation of the pinched plasma column generated in a linear Z-pinch device. The investigation was conducted using a 5 inch cylindrical discharge chamber in which plasma discharges were made in a 70 millitorr argon atmosphere. A well-defined current sheet was formed and collapsed to the center of the discharge chamber as a result of the  $\vec{J} \times \vec{B}$  body force acting on the plasma particles. The current sheet collapsed into a well-defined pinched plasma column of 5 mm radius at 4  $\mu$ sec in which 80 percent of the gas initially in the discharge chamber was entrained. Plasma column lifetime was observed to be approximately 5  $\mu$ sec after which the plasma column boundary expands toward the chamber wall. No detectable MHD instabilities were observed.

Measurement of pressure on the axis using a high speed piezoelectric transducer enabled identification of three regions of characteristic behavior. They were in their time sequence of plasma column development: pressure asymmetry resulting from ion streaming (I), plasma heating manifest in rapid increase in pressure (II), and slight decreasing static pressure in which some heating of the plasma was noted (III).

The pressure asymmetry in region I was attributed to the axial flow of plasma generated by the axial pressure gradient resulting from

nonsimultaneous pinch of the plasma column. Approximately 20 percent of the plasma heating in region II could be attributed to viscous effects introduced by radial gradients in the axial streaming velocity in the column during region I. The remaining heating energy could not be rationalized without reservation. However turbulent heating resulting from excitation of the ion-acoustic wave instability produced by intense electron current flow in the plasma column is considered a possible mechanism. Heating was observed in region III but was of a lesser order than the heating observed in region II.

An energy balance conducted in region I indicated that at least 50 percent of the energy deposited within the discharge chamber was lost by radiation. In regions II and III the percentage of energy loss through radiation was greater. The energy deposited in the plasma, region I, was approximately 25 percent of the discharge chamber energy but only 2 percent of the total capacitor bank energy. Assuming that all of the magnetic field energy was available for accelerating the plasma then the energy transfer efficiency increases to almost 3 percent.

## REFERENCES

1. Jahn, R. G., Physics of Electric Propulsion, McGraw Hill Book Company, New York, (1968).
2. York, T. M., and Jahn, R. G., "Pressure Distribution in the Structure of a Propagating Current Sheet," Physics of Fluids, Vol. 13, No. 5, (1970).
3. Anderson, O. A., et al., "Neutron Production in Linear Deuterium Pinches," Physical Review, Vol. 110, No. 6, (June 1958).
4. Bodin, H. A., et al., "Rapid Compression Heating of a Plasma in the Linear Z-Pinch," Nuclear Fusion, I, (1960).
5. Marshall, J., "Performance of a Hydromagnetic Plasma Gun," Physics of Fluids, Vol. 3, (1960).
6. Jahn, R. G., et al., "Ejection of a Pinched Plasma from an Axial Orifice," AIAA Journal, Vol. 3, (October 1965).
7. Fillipov, N. V., "Investigation of Pressures in a Powerful Pulsed Gas Discharge Using a Piezoelectric Measuring Device," Plasma Physics and the Problem of Controlled Thermonuclear Reactions, Vol. III, Pergamon Press Inc., New York, (1961).
8. Braginskii, S. I., et al., "Theory of Compression and Oscillation of a Plasma Column in a Powerful Pulsed Discharge," Plasma Physics and the Problem of Controlled Thermonuclear Reactions, Vol. IV, Pergamon Press Inc., New York, (1961).
9. Jahn, R. G. and von Jaskowsky, W. G., "Pulsed Electromagnetic Gas Acceleration," Ninth Semi-Annual Progress Report, Princeton University Department of Aerospace and Mechanical Sciences, Report No. 634h, Chapter V, (January 1967).
10. Andrianov, A. M., et al., "Study of a Pulsed Discharge in Deuterium for Current Rates of Rise Up to  $10^{12}$  amperes/sec and Voltages Up to 120kv," Plasma Physics and the Problem of Controlled Thermonuclear Reactions, Vol. IV, Pergamon Press Inc., New York, (1961).
11. Wilbur, P. J. and Jahn, R. G., "Energy Transfer from a Pulse Network to a Propagating Current Sheet," AIAA Journal, Vol. 18, No. 1, (January 1970).

## REFERENCES (Cont.)

12. Ellis, W. R. and Jahn, R. G., "Ion Density and Current Distributions in a Propagating Current Sheet, Determined by Microwave Reflection Technique," Plasma Physics, Vol. 3, (1969).
13. Burton, R. L., "Structure of the Current Sheet in a Pinch Discharge," Ph.D. thesis, Department of Aerospace and Mechanical Sciences, Princeton University, Princeton, N. J., (1966).
14. Black, N. A., "Dynamics of a Pinch Discharge Driven by a High Current Pulse-forming Network," Ph.D. thesis, Department of Aerospace and Mechanical Sciences, Princeton University, Princeton, N. J., (1966).
15. Huddleston, R. H. and Leonard, S. L., Plasma Diagnostics, Academic Press, Inc., New York, (1965).
16. Glasstone, S. and Lovberg, R. H., Controlled Thermonuclear Reactions, Van Nostrand Reinhold Company, New York, (1960).
17. York, T. M., "Stress Dynamics in High Speed Piezoelectric Pressure Probes," Review of Scientific Instruments, Vol. 41, No. 4, (April 1970).
18. Ferri, A., "Fundamental Data Obtained from Shock Tube Experiments," AGARD Report No. 41, Pergamon Press, Inc., New York, (1961).
19. Jahn, R. G. and von Jaskowsky, W. F., "Pulsed Electromagnetic Gas Acceleration," Fourth Semi-Annual Progress Report, Princeton University Department of Aerospace and Mechanical Sciences, Report No. 634c, Chapter II, (July 1964).
20. Drellishak, K. S., et al., "Partition Functions and Thermodynamic Properties of Argon Plasma," AEDC-TDR-63-146, (August 1963).
21. Rosenbluth, M., et al., "Infinite Conductivity Theory of the Pinch," Los Alamos Scientific Laboratory Report LA-1850, Los Alamos, New Mexico, (1954).
22. Roberts, D. E., "Measurement at the Stark Broadening Parameters of Several Ar II Lines," Proc. Phys. Society, Series 2, Vol.1, (1968).
23. Spitzer, L., Physics of Fully Ionized Gases, Interscience Publishers, New York, (1962).

## REFERENCES (Cont.)

24. Tannenbaum, B. S., Plasma Physics, McGraw Hill Book Company, New York, (1967).
25. Knoche, K., et al., "Gas-Plasma Research at the Institute for Thermodynamics, Braunschweig," AGARD Report 320, (September 1959).
26. Folkierski, A., et al., "End Effects in a Linear Z-Pinched Discharge," Nuclear Fusion, 1962 Supplement, Part 2, (1962).
27. Pert, G. J., "Some Observations of a Conical Z-Pinch Discharge," Plasma Physics, Vol. II, Pergamon Press, Inc., New York, (1969).
28. Bernstein, M. J., et al., "Space, Time and Energy Distributions of Neutrons and X-Rays from a Focused Plasma Discharge," Physics of Fluids, Vol. 12, No. 10, (October 1969).
29. Bernstein, M. J., "Acceleration Mechanism for Neutron Production in Plasma Focus and Z-Pinch Discharges," Physics of Fluids, Vol. 13, No. 11, (November 1970).
30. Toepfer, A. J., et al., "Ion Heating in the Dense Plasma Focus," Physics of Fluids, Vol. 14, No. 1, (January 1971).
31. Rudakov, L. I. and Korablev, L. V., "Quasilinear Theory of Current Instability in a Plasma," Soviet Physics JETP, Vol. 23, No. 1, (July 1966).
32. Berger, N. A., et al., "Dynamics of Plasma Heating in a Straight Turbulent Discharge," Soviet Physics JETP, Vol. 29, No. 5, (November 1969).
33. Hamberger, S. M. and Friedman, M., "Electrical Conductivity of a Highly Turbulent Plasma," Physical Review Letters, Vol. 21, No. 10, (September 1968).
34. Glasoe, G. N. and Lebacqz, J. V., Pulse Generators, MIT Radiation Laboratory Series, Vol. 5, Boston Technical Publishers, (1964).
35. Jackson, J. D., Classical Electrodynamics, John Wiley and Sons, New York, (1962).

## APPENDIX A

## DESIGN OF THE PULSE FORMING NETWORK

Ideally, the generation of a constant discharge current pulse, desirable for the present study, can be realized with a lossless transmission line. The basic lossless transmission line consists of distributed capacitance and inductance chosen to be of sufficient magnitude to generate a constant current pulse of desired period and amplitude. The lossless transmission line can be represented by an impedance,  $Z_L$ , (34)

$$Z_L = \left( \frac{L'}{C'} \right)^{1/2} \quad [A.1]$$

when discharged, a current pulse of half period  $\tau$  is generated (34)

$$\tau = 2\ell (L'C')^{1/2} \quad [A.2]$$

The quantities  $L'$  and  $C'$  represent the distributed inductance, henries/meter, and capacitance, farads/meter, respectively;  $\ell$  represents the length of the transmission line. For the present study the capacitance is not truly distributed but rather is lumped. Thus an equivalent pulse forming network must be described that will have the desired ideal transmission line characteristics. Assuming a large number of lumped elements in the circuit, the impedance and half period can be found from

$$Z_L = \left( \frac{L'}{C'} \right)^{1/2} \quad [A.3]$$

and

$$\tau = 2n [L''C'']^{1/2} \quad [A.4]$$

where  $L''$  and  $C''$  are the lumped inductance and capacitance respectively and  $n$  is the number of lumped sections. It should be noted that the capacitance is in parallel and the inductance in series with regard to the load element. Each capacitor element has associated with it an inductance, but due to the fact that this inductance is in parallel with respect to the load, the equivalent contribution was found to be small in comparison to the circuit series inductance. Thus the contribution of the capacitor inductance was neglected.

For the present study,  $n = 10$  was selected as a reasonable number of elements for generating a constant current pulse. This selection was based upon a study, in which, the pulse network application to Z-pinch devices was investigated (14). Circuit capacitance consisted of a series of 10 capacitor units connected in parallel, with 5 microfarads per station and one capacitor at each station. Inductance was distributed, however, and controlled by varying the separation between the flat ground plate and the active conductor. Distributed inductance, which can be converted into lumped inductance for expressions [A.3] and [A.4], was estimated from the parallel plate expression (35) to be

$$L = (4\pi\epsilon_0)^2 \frac{\mu a + \mu_c \delta}{b} \quad [A.5]$$

The quantities  $a$  and  $b$  represent the plate separation and plate width respectively. Also,  $\mu$  and  $\mu_c$  represent the permeability of the material between the plates and the conductors themselves respectively.

Considering the materials used here, copper and nylon,  $\mu$  and  $\mu_c$  are essentially equal to the free space value  $\mu_o$ . The symbol  $\delta$  represents the skin thickness of the conductors to electromagnetic radiation of frequency  $\omega$ . It is given by (35)

$$\delta = \left[ \frac{1}{2\pi\epsilon_o \mu_o \sigma \omega} \right]^{1/2}, \quad [\text{A.6}]$$

where  $\sigma$  represents the plate conductivity. Substitution of the conductivity of copper and the desired current frequency,  $3.14 \times 10^5$  radians/sec, into [A.6] the skin thickness was found to be for this high frequency application

$$\delta \approx 0.03 \text{ cm}.$$

This is more than one order of magnitude less than minimum plate separation, approximately 1 centimeter. Thus from the above discussion [A.5] becomes

$$L \approx \mu_o \frac{a}{b}. \quad [\text{A.7}]$$

Using the minimum plate separation, 0.25 inches, and the width of the active conductor, 2.75 inches, the distributed inductance was found from [A.7] to be

$$L \approx 1.2 \times 10^{-7} \text{ henries/meter}.$$



The length of this section was approximately 2 meters thus the total line inductance,  $L_\ell$ , was

$$L_\ell \sim 2.4 \times 10^{-7} \text{ henries} .$$

A significant source of total circuit inductance arises at the connection between the pulsed network and the discharge chamber switch. An average plate separation was estimated to be 0.75 inches over a 0.75 meter length section of line. This inductance, referred to as the front section inductance,  $L_f$ , was thus estimated to be from [A.7]

$$L_f \approx 2.7 \times 10^{-7} \text{ henries} .$$

Adding  $L_f$  and  $L_\ell$  the total inductance was estimated to be 510 nanohenries. Lumping this into 10 different stations with the capacitors, the circuit impedance and pulse half period were estimated from [A.3] and [A.4] to be

$$Z_L \approx 0.1 \text{ ohms and } \tau \approx 8.8 \mu\text{sec} .$$

The circuit current was approximated as

$$I = \frac{V_o}{Z_L} \approx 10^5 \text{ amperes} , \quad [\text{A.8}]$$

where  $V_o$  was the capacitor bank voltage prior to discharge, 10kv.

Thus the predicted current pulse is constant with a half period of 8.8 $\mu$ sec and a total current of  $10^5$  amperes, almost 50 percent higher than estimated from Figure 2. Both of these differences were attributed to low estimates on line inductance, see [A.3], [A.4] and [A.8], as well as limitations on the theoretical model. Difficulty was encountered in

estimating the front section inductance. If the front section inductance was increased such that half periods matched then the pulsed current predicted from [A.8] would be 87ka which is closer to the current 70ka, estimated from Figure 2. The remaining discrepancy was attributed to the theoretical model adopted here.

It should be noted that the impedance contribution of the discharge chamber and switch were not included in the above analysis. This follows from established parameters in similar configurations (14) with the pulse network having a much greater impedance than the discharge chamber and switch. As a result the effect of the current sheet dynamics on the circuit current waveform is small in comparison to the pulse network. Thus the plasma dynamics and pulse network are essentially uncoupled enabling application of the above simple analysis to obtain estimates of the circuit current behavior. Consideration will now be given to this small discharge chamber-switch impedance assumption.

The impedance of the discharge (discharge chamber plus switch),  $Z_D$ , is equal to the total voltage drop across the chamber divided by the total circuit current (11)

$$Z_D \approx R_D + \frac{dL_D}{dt} + \frac{L_D}{I} \frac{dI}{dt} , \quad [A.9]$$

where  $R_D$  is the resistance of both the switch and discharge chamber and  $L_D$  is the discharge chamber inductance. Switch inductance effects were not considered important due to the presence of a pinch inhibiting plexiglas insert in the switch.

The discharge chamber inductance was estimated from the standard coaxial relationship

$$L_D = \frac{\mu_o h}{2\pi} \ln \frac{c}{r} , \quad [A.10]$$

where  $c$  is the radius of the aluminum return conductor. At pinch,  $L_D$  is a maximum and was estimated to be

$$L_D \approx 20nh .$$

From [A.10]

$$\frac{dL_D}{dt} = \frac{\mu_o h}{2\pi r} \frac{dr}{dt} \quad [A.11]$$

Using [A.9], [A.10] and [A.11] the impedance of the current sheet at 1 inch was found to be approximately

$$Z_D \approx 25 \text{ milliohms} ,$$

roughly 0.25 the pulse network impedance, 100 milliohms. At pinch the discharge impedance was (14)

$$Z_D \approx 5 \text{ milliohms} ,$$

where the second and third terms in [A.9] are zero. Thus it can be seen that the pulse network impedance will be 4 to 20 times as great as the discharge impedance except just prior to pinch. In the case just prior to pinch the second term in [A.9] becomes large in which case the ratio of line impedance to discharge impedance drops to two. Thus, except just prior to pinch, the discharge current is effectively uncoupled from the discharge dynamics. This is in agreement with the

current waveform behavior depicted in Figure 2 although no indication of a large impedance effect near pinch was noted.